**Simulation of Pickup ions - Local Interstellar Medium
Interactions in the Outer Heliosphere**

by

Ding Sheng

A dissertation submitted to the Graduate Faculty of
Auburn University
in partial fulfillment of the
requirements for the Degree of
Doctor of Philosophy

Auburn, Alabama
December 11, 2021

Keywords: Heliopause, Interstellar plasma, Pickup ions

Approved by

J. D. Perez, Chair, Professor of Physics
Yu Lin, Professor of Physics
Kaijun Liu, Professor of Physics
David Maurer, Professor of Physics
Hong Zhao, Assistant Professor of Physics

Abstract

The energetic neutral atoms (ENAs) received by Interstellar Boundary Explorer (IBEX) shows a ribbon structure of the ENA source around the heliopause, the plasma boundary of solar system. The reason behind it is still a mystery. Hybrid simulations in two-dimensional space and three-dimensional velocity dimensions with continuous injection of pickup ions (PUIs) discussed in this dissertation provide insight into the plasma processes that are responsible for the pitch angle scattering of PUIs outside the heliopause. The isotropization time of the PUIs is estimated and discussed in relation to two variants of the secondary ENA mechanism as an explanation of the IBEX ENA ribbon, showing the time is too short for the conventional model and providing ground for further studies.

Acknowledgments

Thanks to all the people who supported and helped me during my PhD study and especially during this harsh time of pandemic. I am deeply grateful to my supervisor Prof. J. D. Perez for his encouragement, kindness and patience. I would like to thank Prof. Kaijun Liu, Prof. Vladimir Florinski and again Prof. J. D. Perez. The work described in this dissertation would not be possible without their help.

Table of Contents

List of Tables

List of Figures

List of Abbreviations

VLISM   Very local interstellar matter

ISMF   Interstellar magnetic field

PUI   Pickup ions

ENA   Energetic neutral atoms

IBEX   Interstellar Boundary Explorer

LISM   Local interstellar matter

PIC   Particle-in-Cell

MHD   Magnetohydrodynamics

Chapter I. Introduction

1. Preface

The dissertation focuses on PUI-VLISM interactions in the outer heliosphere. The background information and general method of simulation are discussed in Chapter I. The accomplished simulations for pickup ions and the results are discussed in Chapter II.

2. Physics of the heliosphere

2.1 The Sun

In order to understand the environment and the physics of the solar system, we begin with the properties and the structure of the Sun. The Sun is a G-type main-sequence star which is about half a billion years old. It has a mass of approximately 2×10^{30} kg, about 3.3 million times of the Earth, and it has a radius of about 7×10^5 km. The Sun consists of 73% of hydrogen and 25% helium. The remaining 2% consists of other heavier elements, of which the heaviest is Uranium.

The Sun has a complex structure that is divided into many layers (Figure 1). There is a hot and dense core, the radiative zone, the convective zone, the subsurface flow and the atmosphere, in the order of increasing distance from the center. The lowest layer of the solar atmosphere is the photosphere. With a temperature of about 6000 K and higher density than other layers of the atmosphere, it is the layer of the sun that radiates light and normally is seen by the human eye. The second layer is the chromosphere, which can only be seen during the solar eclipse. The outside layer is called the corona. It has a very high temperature (10^6 K), very low density, and extends far from the Sun. The corona plays a key role as the source of the solar magnetic field and the solar energetic particles that constitute the solar wind which fills the solar system and eventually interacts with interstellar space.
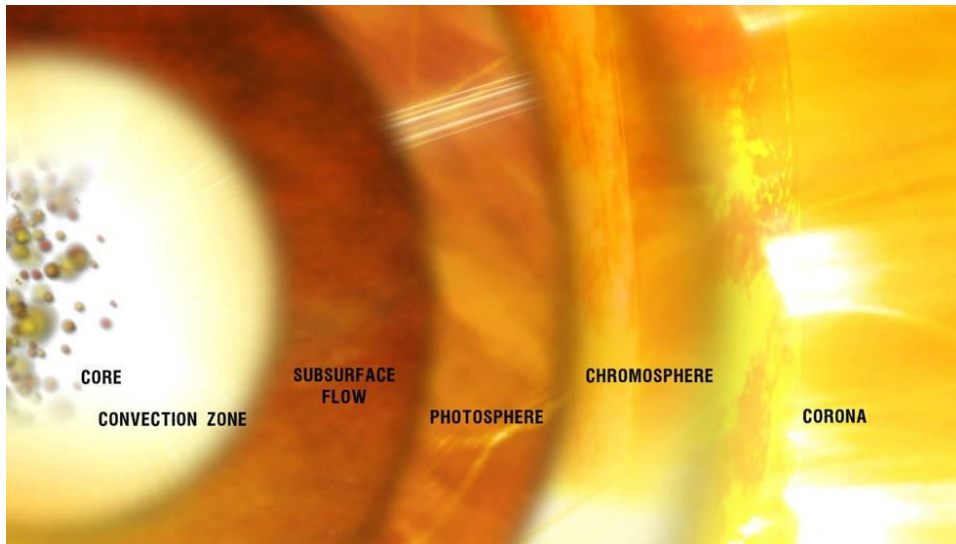
Figure 1. Layers of sun. (Image credits: NASA's Goddard Space Flight Center)

The surface rotation rate of the Sun varies with latitude. It rotates faster at the equator (about 24 days), and slower at the poles (more than 30 days), On average, it is 27 days. The rotation twists the magnetic field into the shape of an Archimedean spiral in space, as the solar wind carries it through the solar system.

The differential rotation results in a quasi-periodic process of the solar magnetic field (explained by solar dynamo theory). About every 11 years, the magnetic polarity of the Sun is flipped and the strength of solar activity, such as sunspot, solar flare, corona mass ejection (CME) and solar radio bursts reach their maximum. The solar activity then decreases to a minimum in the next half of the 11-year period. This quasi-periodical behavior is called the solar cycle. It is quasi-periodical, as the duration varies (9-14 years) and the activity for each solar cycle can be quite different (Figure 2). The solar minimum is usually a quiet period for the sun with few sunspots and flares observed for weeks, meanwhile, the intensity of galactic cosmic rays that reach the earth rises ~20% during solar minimum (Figure 3) as the magnetic field in the heliosphere is weaker.
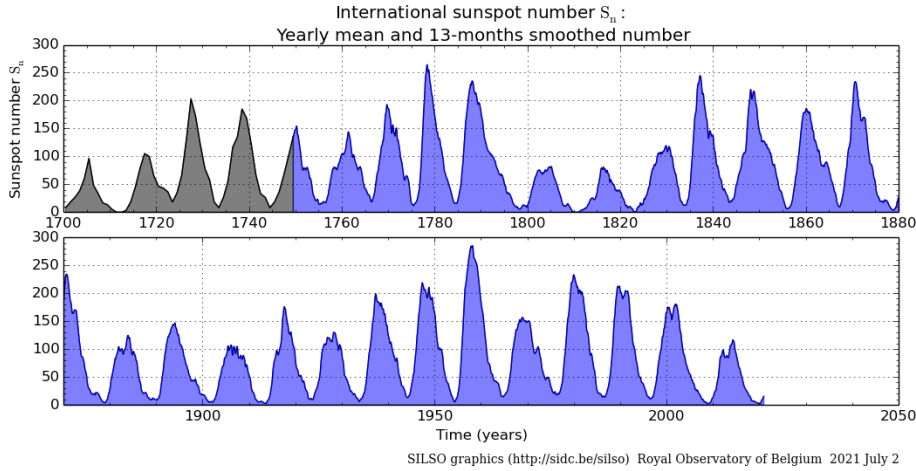
Figure 2. Yearly mean sunspot number (black) up to 1749 and monthly 13-month smoothed sunspot number (blue) from 1749 to the present. (Image credit: SILSO)
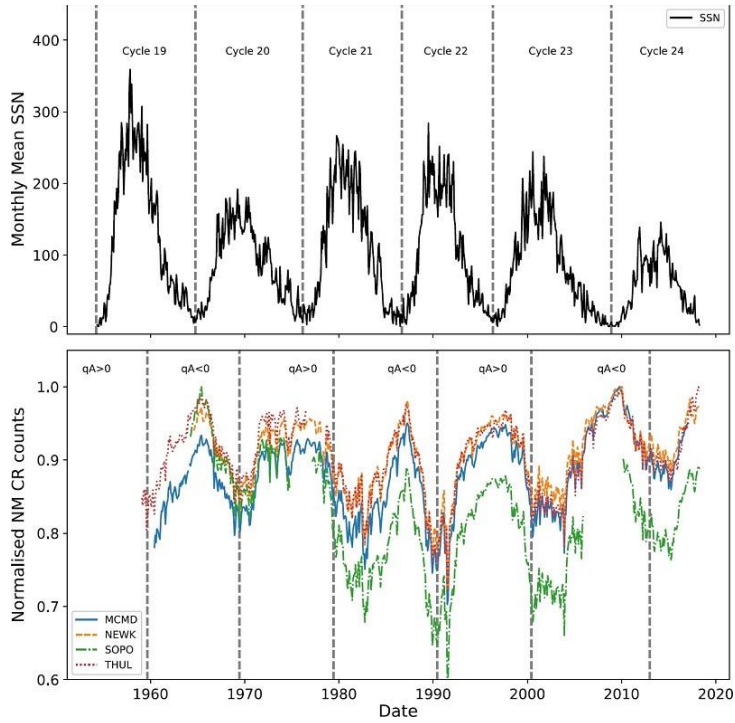
Figure 3. Sunspot number (SSN) (top), with vertical lines showing the beginning of each solar cycle. Cosmic ray (CR) intensity recorded by neutron monitors (NMs) (bottom), with vertical lines showing the approximate epochs of solar magnetic-field polarity reversals. (MCMD = McMurdo, NEWK = Newark, SOPO = South Pole, THUL = Thule). (Ross, 2019)

2.2 The Solar Wind

The solar wind is a flow of charged particles generated in the solar corona and released into space, along with "open" magnetic field lines which extend into the deep space far from the Sun. It consists of a hot plasma with 96% proton and 4% He^{2+}, as well as a small fraction of heavy ions. The fraction is dependent on solar wind speed, the faster the solar wind, the higher percentage of helium. The mass loss of the sun due to the solar wind, 10^9 kg/s, is about 1/4 times the mass loss due to the emission of the photons, while the dynamic pressure of the solar wind is several orders of magnitudes larger than the radiation pressure of the photons. The solar wind is the linkage between the sun and the entire solar system. It interacts with the planetary fields and the ionosphere/atmosphere and the surface of the planets. Finally, it interacts with the interstellar medium and interstellar magnetic field determining the structure of the heliosphere.

There are two different kinds of solar wind with different speeds, the low-speed streams (~400 km/s) and the high-speed streams (1000~2000 km/s). Both streams are super-Alfvénic and supersonic when they are observed near Earth (1AU). The interaction between them increases with distance from the sun, reducing the range of velocity distributions. The low-speed streams are constantly generated from coronal streamers, a bright cap-like structure normally at the lower latitudes of the sun. The high-speed streams are released from coronal holes, large, dark, low-density regions in the corona, occasionally found near the poles (Figure 4). A coronal hole rotates at about a 27-day rate, so the high-speed solar wind it generates can cause repeated geomagnetic storms on earth. During solar minimum, when the sun is calm, the coronal hole tends to be more stable and to extend farther from poles, and the high-speed streams become stronger and dominate at high latitude. During solar maximum, the corona holes disappear, and

the magnetic polarity of the sun becomes irregular. The solar wind density is increased because of solar activity, while the average speed of solar wind is decreased due to fewer high-speed streams. (Figure 5)
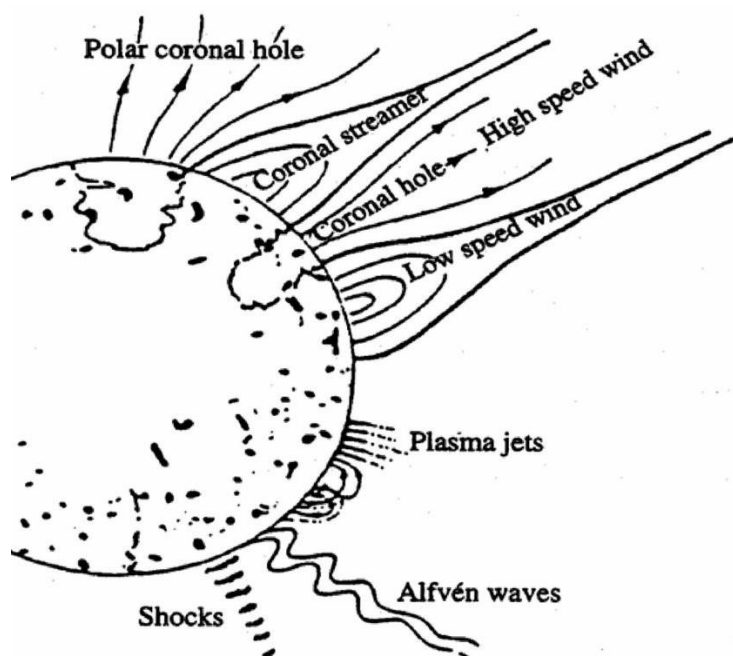
Figure 4. Drawing of the sun, representation of the fast solar wind connected to the open magnetic field lines from coronal holes and the slow wind associated with coronal streamers above coronal loops. (Dryer, 1987)
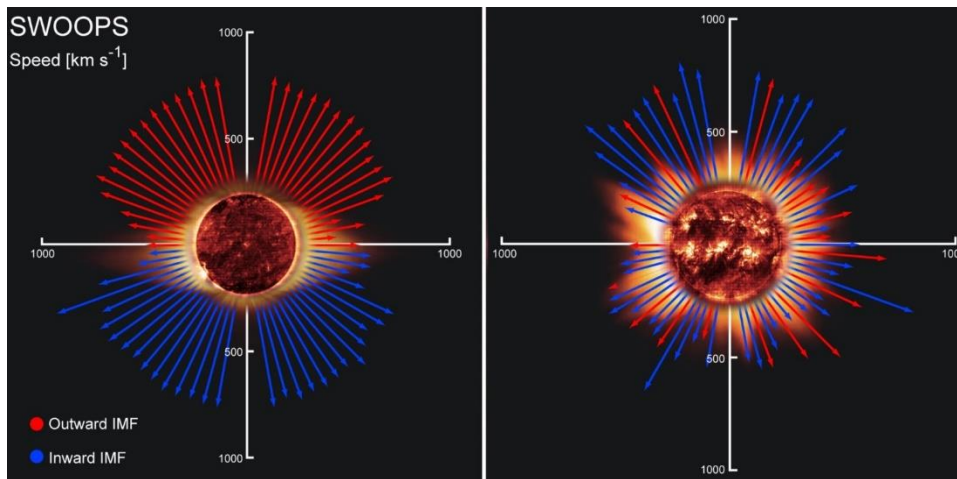
Figure 5. Polar plot of solar wind speeds measured by Ulysses. At solar minimum (left panel) the fast wind fans out from the poles to fill two thirds of the heliosphere, blowing at an average uniform speed of 750 km/s (see arrows), much faster than the wind that emerges from the Sun's equatorial zone at 350 km/s. At solar maximum (right panel) the solar wind is more turbulent and irregular. (Image credit: ESA)

2.3 The Interstellar matter and Interstellar magnetic field

The solar system travels around the center of the Milky Way Galaxy for about 225 to 250 million years per cycle. In the last thousands of years, it moved in a local interstellar cloud (Figure 6), which lies in a cavity referred to as the local bubble, with a speed of the order 25 km/s. The local bubble is at least 300 light-years across, connected with the Loop I Bubble. Both lie in the Orion spur between Carina–Sagittarius Arm and the Perseus Arm of the Milky Way. The local bubble has a density of 0.05 atoms/cm^3, which is about 1/10 of the average density of the Milky Way. It may have been generated by bursts of supernovae millions of years ago.
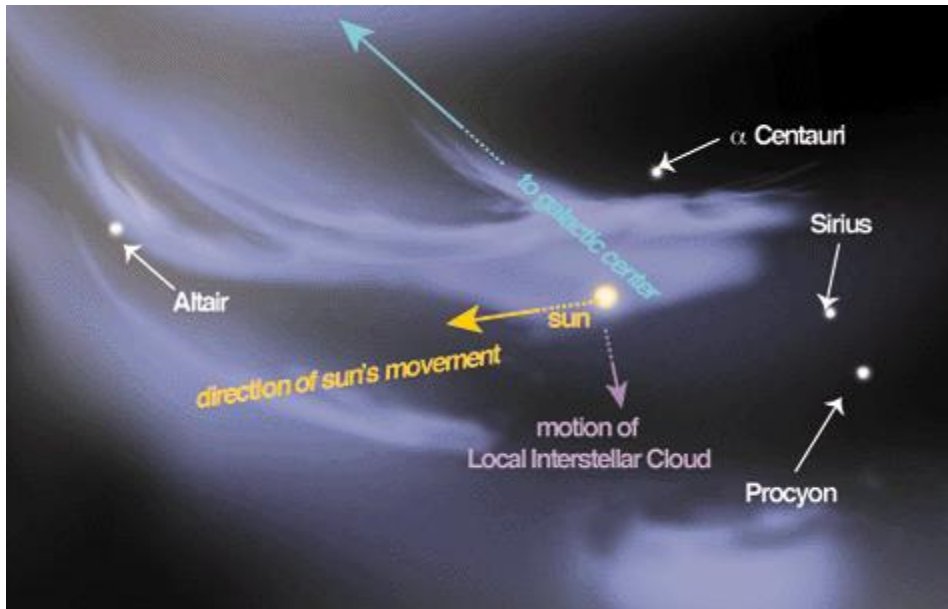
Figure 6. The local interstellar cloud. (Image Credits: Linda Huff, Priscilla Frisch (U. Chicago))

The local interstellar cloud, with an unknown origin, has a density of 0.3 atoms/cm^3, higher than the local bubble. It consists of about 99% gas and 1% dust. Of the gas, 91% is hydrogen and 8.9% is helium (Ferrière, 2001). The interstellar matter that surrounds the solar system, referred to as the very local interstellar matter (VLISM), is typically from the local interstellar cloud but may also contain elements from other clouds nearby.

As most of the interstellar medium is ionized, it is coupled with the interstellar magnetic field (ISMF) generated in the galaxy. Various observations, like the Faraday rotation of the linear polarization of starlight, have shown the structure of the galactic magnetic field. The Milky Way has a large-scale spiral magnetic field that follows the structure of the galaxy, as well as small scale fluctuations. While there is a stronger field in the galactic center (Ferrière, 2009), the average field strength of the galactic disk is a few of μG (Ferrière, 2001). The local ISMF close to the solar system, as confirmed by the observation of the Interstellar Boundary Explorer (IBEX, see section 4), is a nearly uniform magnetic field of ~3μG with the field vector pointing

towards the galactic coordinates longitude $\ell = 47° \pm 20°$, latitude $b = 25° \pm 20°$ with a weak curvature of $0°.25\ pc^{-1}$ (Frisch et al. 2012).

2.4 The Heliopause

The solar wind particles generated by the sun expand in a cavity called the heliosphere, until they meet and interact with the VLISM and ISMF. As the solar wind expands outward approaching the flow of the VLISM, a termination shock (~100 AU from the sun) is formed where the solar wind is heated and compressed. When the solar wind passes through the heliospheric termination shock, it transits from supersonic to subsonic, but remains super-Alfvénic. Further out is the boundary between the sun's magnetic field and the ISMF called the heliopause (~120 AU from the sun), where both magnetic fields are bent and compressed around the heliosphere. The compressed magnetic field at the heliopause stops and separates the ions from the solar wind (it is no longer super-Alfvénic there) and the VLISM. The neutral atoms from the VLISM and solar wind, however, do not stop, but penetrate the heliopause. The region between the termination shock and the heliopause contains solar wind plasma that has been slowed from supersonic to subsonic. This region is called the inner heliosheath. The region just outside the heliopause is often referred to as the outer heliosheath. Note that the heliopause is often regarded as the boundary of the solar system, despite the fact that the range of the gravitational pull of the sun extends much further, to the Oort cloud (thousands of AU from the sun) where comets originate.

Although Voyager 1 and Voyager 2 have crossed the heliopause in the upstream direction (Voyager 1: at 121 AU from the sun on August 25, 2012, Voyager 2: at 119 AU from the sun on November 5, 2018, NASA JPL. n.d.), the global shape of the heliopause is still unknown. In the conventional model, it has the shape of a comet, with a round nose upstream and a long tail

downstream. A recent magnetohydrodynamics (MHD) simulation (Opher et al, 2020) suggests

that the heliopause has a compact croissant-like shape, round in the upstream, and has a complex

structure downstream (Figure 7).
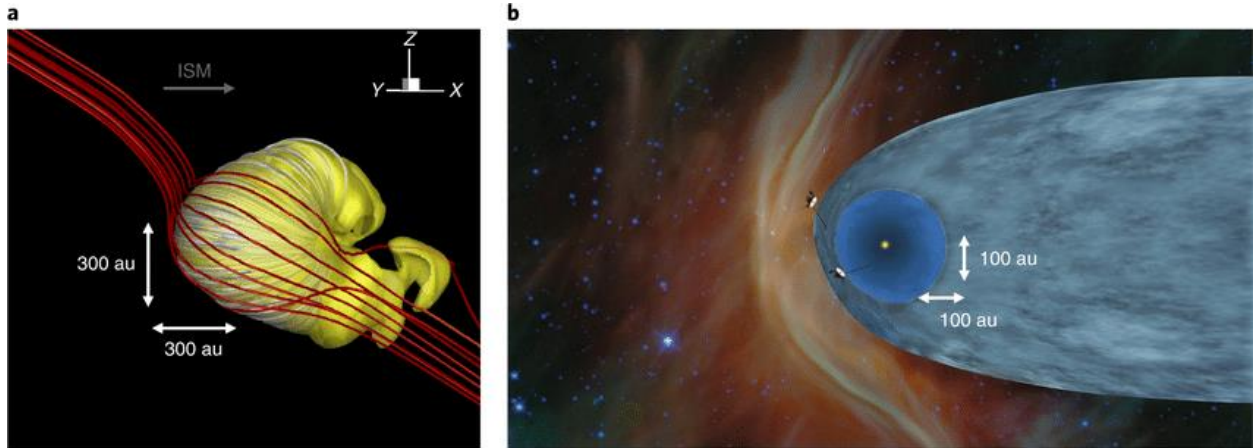
Figure 7. Left (a): new model of heliopause, yellow surface represents heliopause, white lines

represent solar magnetic field, redlines represent interstellar magnetic field. Right (b): Artistic

drawing of conventional model of heliopause with voyager 1 and voyager 2. (Opher et al, 2020)

People once believed that there is a bow shock structure in the upstream position outside the

heliopause, like the bow shocks of planets outside the magnetosphere or ionosphere. Studies

based on IBEX (we will discuss it in Section 3) suggest that there is no bow shock at all.

2.5 Pickup ions

The term pickup ions (PUIs) describe various species of ions in space plasmas with a common

feature described by their name. A pickup ion begins as a neutral atom unaffected by the

magnetic field then becomes an ion in a charge exchange reaction and then is picked up by

streams of local plasma and trapped by its magnetic field. There are two species of pickup ions

associated with the interaction between the solar wind and interstellar matter. These pickup ions play important roles in forming the shape of the heliopause.

The interstellar pickup ions found inside the heliopause have been observed between 1.35 and 5.4 AU by the robotic space probe Ulysses. A weak pitch-angle scattering and a broad range of ions including H, He, N, O, and Ne (Gloeckler and Geiss, 1998) are present. They originate in the interstellar neutral gas that penetrates the heliosphere a few AU outside the sun, where they are photoionized by solar photons, or ionized by the charge exchange process as they flow into the supersonic solar wind. The ionized particles are then picked up by solar wind. The spatial distribution of the interstellar pickup ions is determined by the flux of interstellar neutral gas, as their trajectories are bent by the gravity and the radiation pressure of the sun. For neutral Hydrogen, it leaves a parabolic depleted zone called the ionization cavity (Zank, 1999), while the heliosphere beyond the cavity is thermally dominated by the PUIs. For heavy neutral atoms like Helium, the effect of radiation pressure is weak compared to gravity, so it piles up downstream from the Sun, leaving a high-density region called the focusing cone (Zank, 1999).

The species of pickup ions we are specifically interested in is the pickup ion outside the heliopause, whose properties are less known and are predicted based on the study of interstellar pickup ions inside the heliopause. Originally, it is the neutral solar wind, a species of energetic neutral atoms (ENAs) generated from solar wind ions as the result of the charge exchange process with the interstellar neutral gas. The neutral solar wind travels across the heliopause and is re-ionized outside the heliopause. The generated ions are then picked up by the ISMF. These pickup ions will be further discussed in Section 3.

3. IBEX and IBEX Ribbon

3.1 The Interstellar Boundary Explorer

In 2008, NASA launched the Interstellar Boundary Explorer (IBEX), a satellite that operates in a highly elliptical earth orbit (NASA, 2019). With a perigee of 47,000 km and an apogee of 308,000 km, it avoids any interference from the radiation belt and magnetosphere of the earth (Figure 8). The IBEX is equipped with two sensors, IBEX-Hi (detects particle with energy range from 0.3~6 keV) and IBEX-Lo (energy range from 0.01~2keV). The purpose is to detect ENAs from the boundary between the solar system and interstellar space and to generate full sky maps in order to understand what is going on in this region of space. The full sky map of ENAs shows a vast unexpected structure of ENA emissions (Figure 9) called the IBEX ribbon (Funsten et al., 2009a; Fuselier et al., 2009; McComas et al., 2009a, 2009b; Schwadron et al., 2009a).
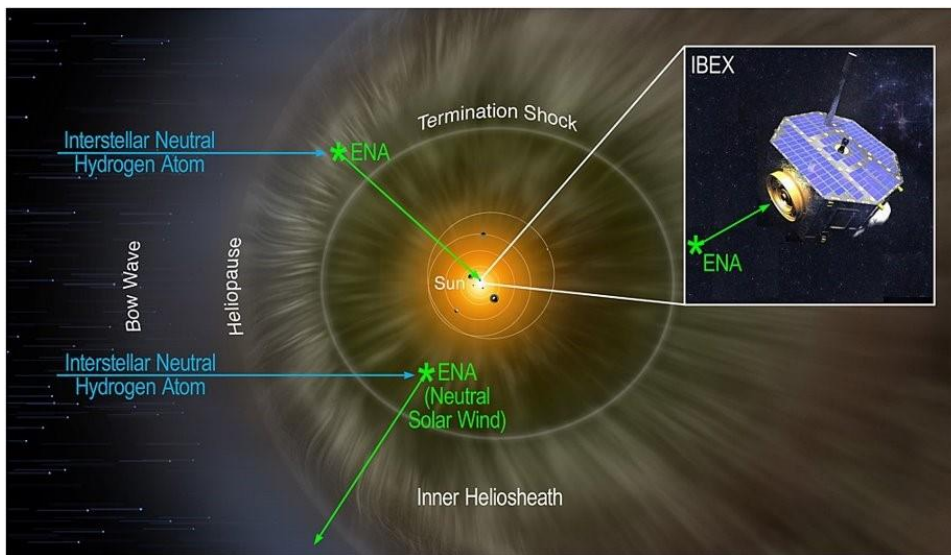
Figure 8. Illustration of Heliosphere by Adler Planetarium; IBEX spacecraft by NASA/Goddard Space Flight Center (GSFC) Conceptual Image Lab.
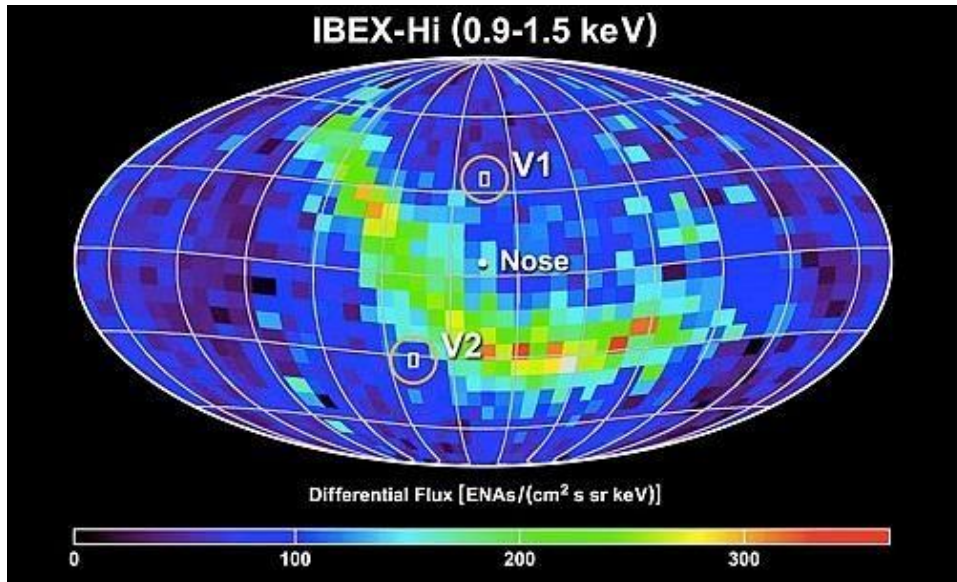
Figure 9. IBEX's all-sky map of energetic neutral atom emission, with the location of the Voyagers (V1, V2) where they cross the terminal shock. The map uses a Mollweide projection and is centered on the nose of the heliosphere at $(\lambda, \beta) = (259°, 5°)$ in ecliptic coordinates, as viewed looking upwind from the Earth. The downwind viewing direction, in the direction of the heliotail, is toward $(\lambda, \beta) = (79°, -5°)$; the poles are at ecliptic latitudes $\beta = \pm 90°$. (Image credit: NASA, SwRI)

3.2 Properties of the IBEX Ribbon

The ribbon is almost circular enhanced ENA emissions around the sky, centered on ecliptic (221°, 39°), with a breach of about 60° in the direction of galactic north (Funsten et al., 2009b; McComas et al., 2009b). The MHD model of Pogorelov et al. (2009) and Schwadron et al. (2009b) suggests that the ribbon direction is perpendicular to the ISMF that is wrapped around the heliosphere (illustrated as Figure 10).
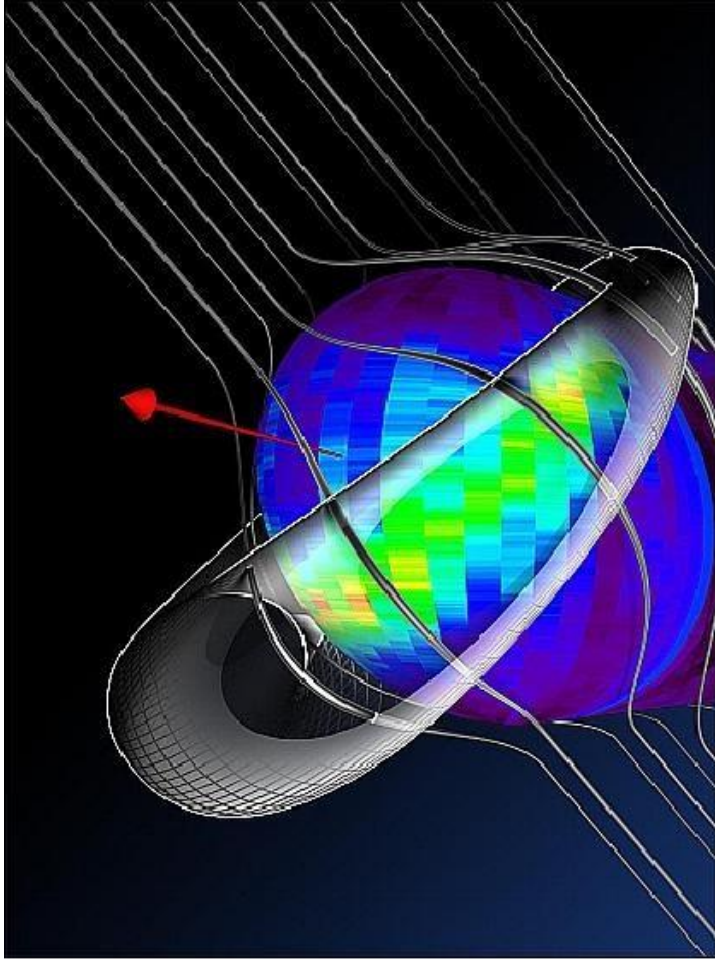
Figure 10. A 3D diagram of the IBEX ribbon image, the silver lines represent the ISMF around heliosphere, the toroid is the region of outer heliosphere related to IBEX ribbon, the red arrow is the moving direction of the Sun. (Image credit: IBEX Team)

McComas et al. (2014, 2017, 2020) summarized the special features of the IBEX ribbon. The latitudinal dependence of ribbon energies is correlated with the solar wind speed structure during solar minimum (Figure 11). The average width of the ribbon is 20°, and it is slightly wider for the component of ENAs with higher energies (also in Figure 11). Full solar cycle variance of the ribbon (Figure 12) shows that the flux of ENAs changes with the same period as the solar cycle but with 2~3 years delay.
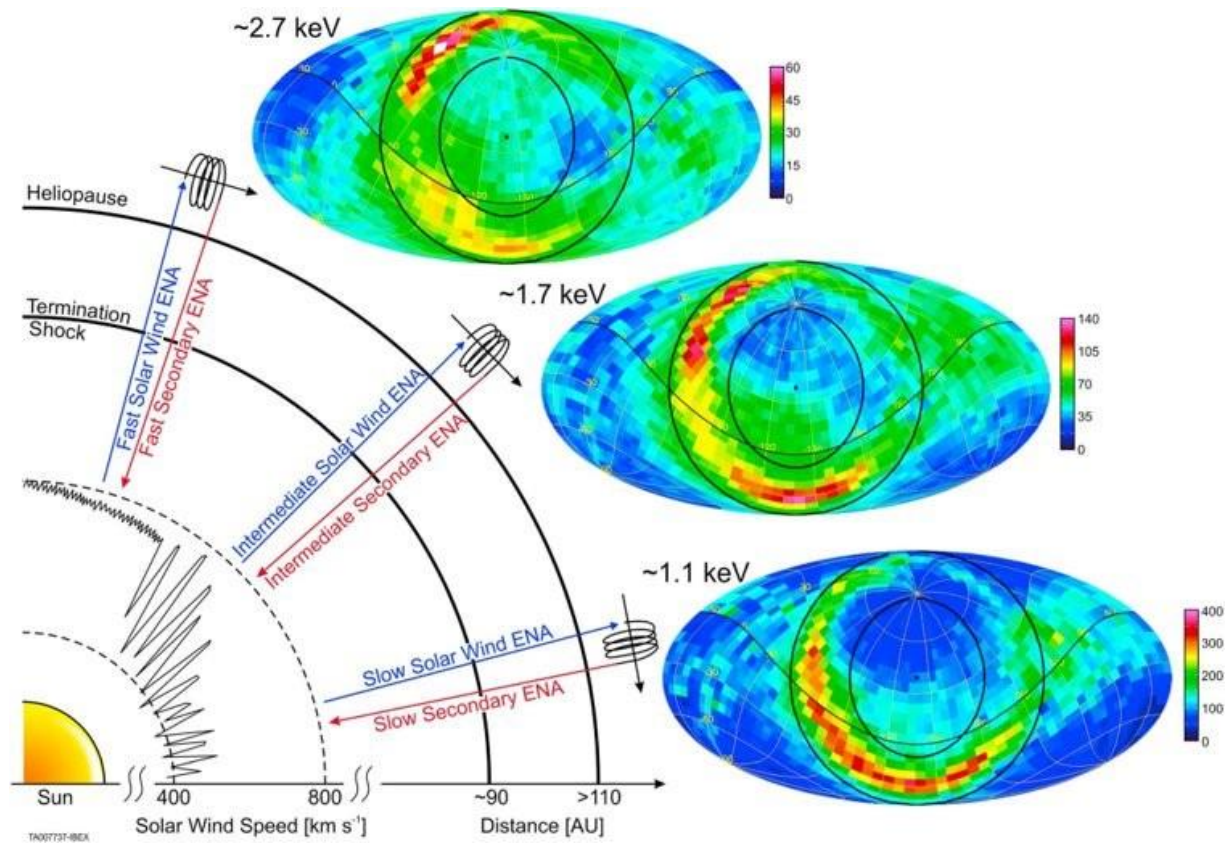
Figure 11. All-sky Mollweide projection maps of the ribbon, centered to ribbon direction, at three different energies compared with a schematic illustrating the solar wind speed structure around solar minimum as determined from Ulysses measurements. Black circles marking the ribbon. Black line marking the location of the ecliptic. Color indicates emission intensity in units of differential ENA flux $(cm^2 \; s \; sr \; keV)^{-1}$ (McComas 2014)
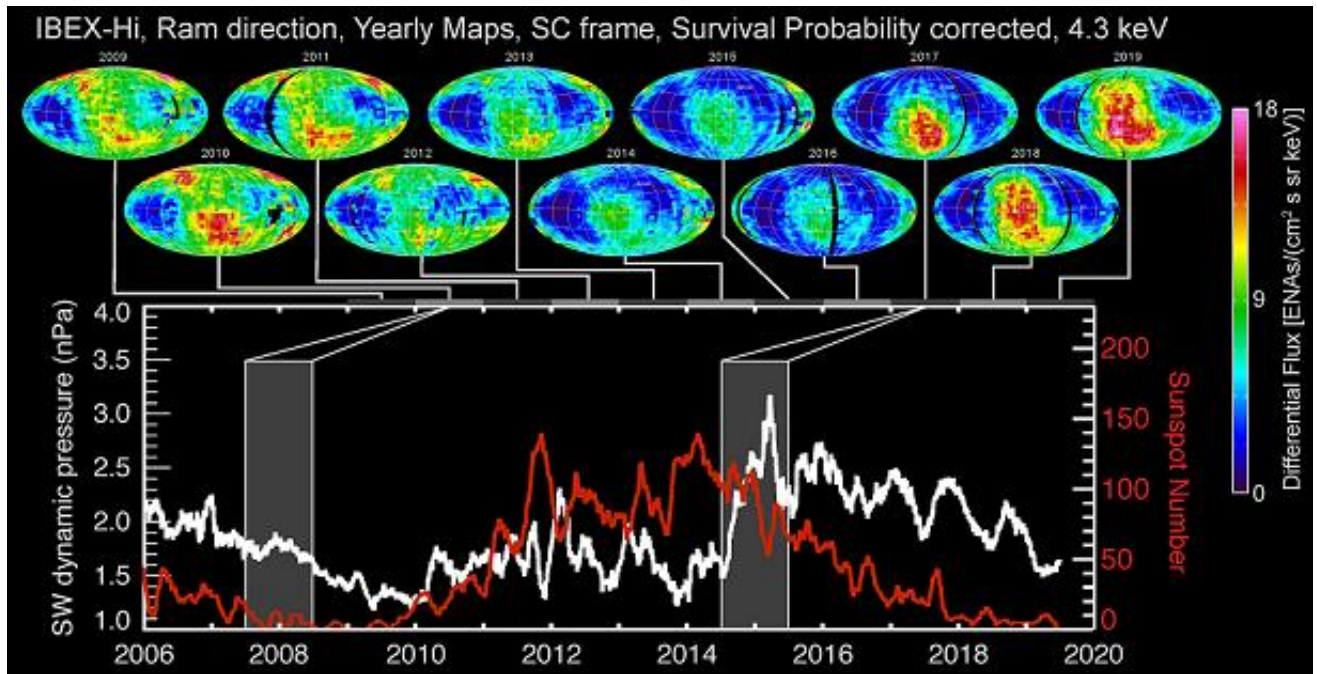
Figure 12. A Full Solar Cycle of Interstellar Boundary Explorer (IBEX) Observations. On top are yearly IBEX images. The bottom panel shows the solar cycle of sunspot number and solar wind dynamic pressure (nPa). (McComas 2000) https://iopscience.iop.org/journal/0067-0049/page/full-solar-cycle-ibex

3.3 Theories about IBEX Ribbon

The properties of the IBEX ribbon described in Section 3.2 place severe restrictions on theories of its origins and our ability to model or simulate its features. Several possible explanations for this very surprising feature of the IBEX observations (Figure 13) have been put forward. They are described and their strengths and weaknesses have been listed in McComas et al. (2014). Our investigations focus upon the model (Figure 14) of a secondary ENA source for the ribbon (McComas et al., 2017; Dayeh et al., 2019; Schwadron and McComas, 2019).
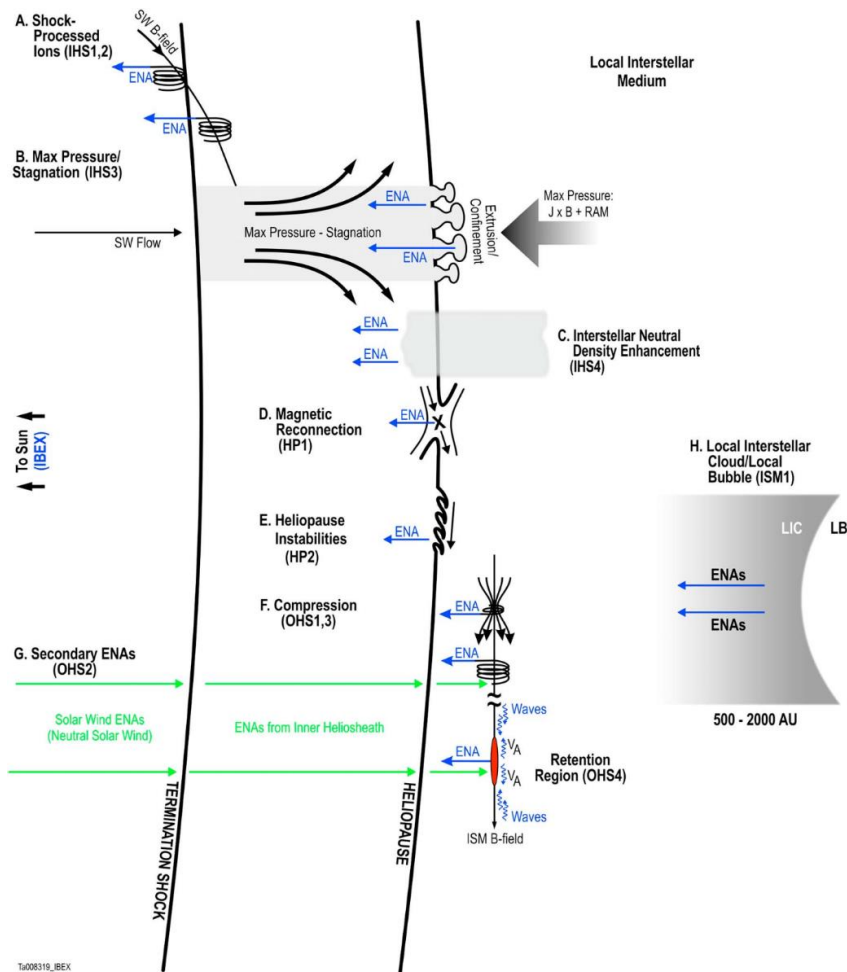
Figure 13. Schematic illustrating the different hypotheses that have been put forward to explain the Ribbon, organized according to formation region. (McComas, 2014)
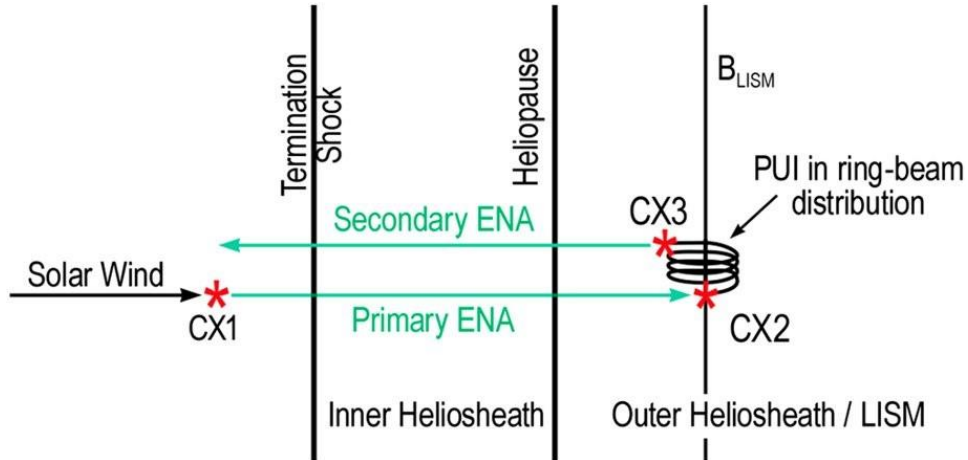
Figure 14. Schematic illustrating ENA production in the outer heliosheath. (McComas, 2014)

The original version was suggested by McComas et al. (2009b). It was subsequently modeled

using a ring distribution of PUIs by Heerikhuisen et al. (2010), Chalov et al. (2010), Möbius et

al. (2013), and Zirnstein et al. (2016, 2018). In this mechanism (Figure 15), at first solar wind

protons charge exchange with interstellar neutrals in the heliosphere and become solar wind

neutrals. After that they pass through the heliopause undeflected. They then charge exchange

again with the interstellar ions in the outer heliosheath, becoming PUIs. Next, they are trapped

on magnetic field lines in the VLISM (or LISM for short) with perpendicular pitch angles,

forming a ring velocity distribution in the ribbon direction. After a long time (characteristic

charge-exchange timescale $\tau_{ex} \approx 6{\times}10^7$ s (~ 2 years)), a portion of PUIs become the secondary

ENAs through a third charge-exchange process with LISM neutrals. The secondary ENAs

penetrate through the heliopause and can be observed by IBEX if they have velocities

antiparallel to the line-of-sight **r**. Thus, for this process to explain the IBEX ribbon at the

observed flux level, the ring distribution must remain stable for a time of approximately 2 years

(Heerikhuisen, 2010).
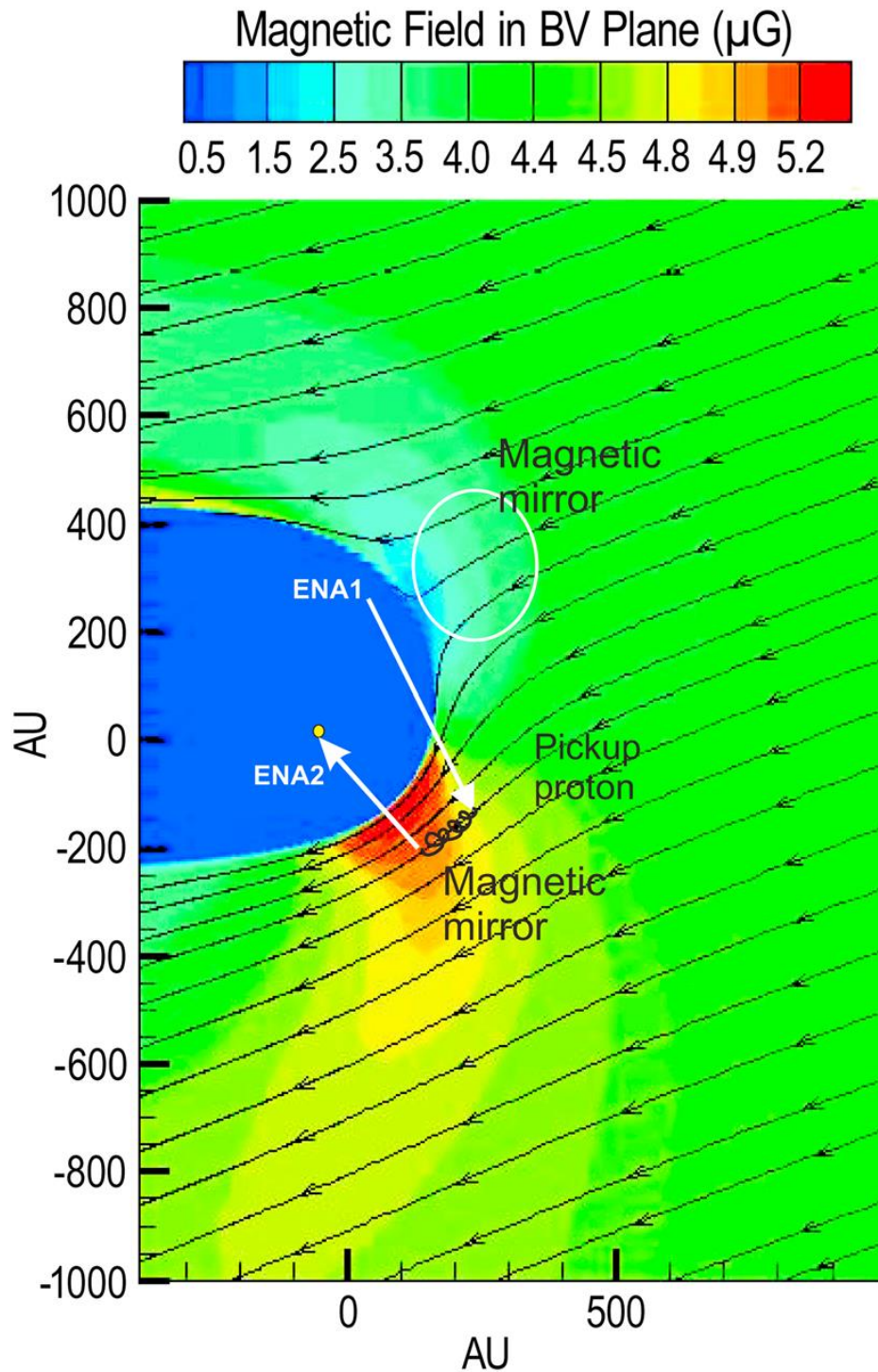
Figure 15. The spatial distribution of the interstellar magnetic field around the heliosphere, calculated with a 3-D kinetic-MHD model of the solar wind/LISM interaction. The x and y axes show the heliocentric distance in AU. The arrows indicate the direction of the ISMF in the plane

that contains the ISMF (**B**) and LISM plasma velocity (**V**) vectors. The color scale gives the magnitude of the field. The figure illustrates the formation of secondary ENAs from mirroring PUIs in regions where the field is compressed against the heliopause. From Chalov et al. (2010).

The main challenge for the secondary ENA model is the scattering of the PUIs ring distribution due to wave-particle interactions. As the pitch angles of PUIs are scattered by plasma instabilities such as the Alfvén ion cyclotron waves, the mirror mode, and the Ion Bernstein wave (Min, 2018), the velocity distribution of PUIs eventually becomes isotropic. In this case, there would be no narrow ribbon structure. This is indeed what previous studies have indicated.

On the other hand, there is a variant of the secondary ENA model (Schwadron and McComas, 2013) that does not depend on the stable velocity distribution. It involves the idea of a spatial retention region, that the PUIs in the ribbon direction are quickly scattered and are frequently reflected by magnetic field variations. It also requires weak scattering outside that region so that the PUIs there drift away. So that, there is higher PUIs density in the ribbon direction due to PUIs flowing in along the magnetic field, building up enough flux to explain the ribbon observations (Isenberg, 2014; Giacalone and Jokipii, 2015). Schwadron and McComas (2019) suggested this as a unifying explanation of the IBEX ribbon.

Note that a fundamental distinction between the two versions of the secondary ENA mechanism is that the original version requires the long-term stability (on a timescale of the order of years) of the PUIs in the ribbon direction, whereas version 2 relies on PUI scattering (also on a timescale of the order of years) to create the needed spatial retention in a region where the radial line of sight **r** is within ±10° perpendicular to the interstellar magnetic field **B**.

4. Plasma simulation method

4.1 Particle in Cell method

Kinetic effects in a plasma are important when the velocity distribution of the particles is non-Maxwellian. It either becomes necessary to trace each particle and the interactions between the particles or treat the statistical behavior of the plasma by solving the Vlasov equation

$$\frac{\partial f}{\partial t} + \mathbf{v} \cdot \nabla_r f + \frac{q}{m}(\mathbf{E} + \mathbf{v} \times \mathbf{B}) \cdot \nabla_v f = 0 \tag{1}$$

coupled with the Maxwell equations,

$$\nabla \cdot E = 4\pi\rho$$
$$\nabla \cdot B = 0$$
$$\nabla \times E = -\frac{1}{c}\frac{\partial B}{\partial t}$$
$$\nabla \times B = \frac{4\pi\mathbf{j}}{c} + \frac{1}{c}\frac{\partial E}{\partial t} \tag{2}$$

where f is the phase-space density, v is the velocities of particles, q is the charge of particle , m is the mass of particle, E is the electric field, B is the magnetic field. The charge density $\rho = \sum_s q_s \int f\, d^3\mathbf{v}$ and the current density $\mathbf{j} = \sum_s q_s \int f\, \mathbf{v} d^3\mathbf{v}$, by summing all the species with index s. In this treatment, the short range 2-body collisions among particles are ignored, i.e., we treat a collisionless plasma. As the phase-space density function $f(\mathbf{r},\mathbf{v},t)$ in Vlasov equation has 7-dimensions, the computational power and memory required to directly solve the equation are unrealistically high for this problem.

The Particle-in-Cell (PIC) method is a discrete approach to the Vlasov equations. It introduces Lagrangian super-particles to represent many particles with a similar phase space position at any time. The velocities, positions and other properties of the super-particles are then traced as real

numbers for each timestep, which can be solved through the equations of motion. On the other hand, continuous properties of the plasma like the self-consistent electric field and magnetic field are solved on a discrete Euler mesh (normally rectilinear grids) simultaneously. Spatial interpolation is used to link both frames together. For example, the charge density and current density on any grid point are calculated by summing all the super-particles in the nearest cells, with a weighting factor related to their distances from the grid point. Similarly, the effect of electric and magnetic fields on any super-particle is interpolated from the fields in all corners of the cell that the super-particle occupies.

The mass ratio between ions and electrons (m_i:m_e = 1836Z:1) is a very large number. It requires a very small timescale and a very large spatial dimension to contain both motions. It is thus necessary to use an artificial mass ratio to save computation time. Other methods like gyrokinetic simulations or hybrid kinetic-MHD method can be used to approximate the full-kinetic solution with limitations.

4.2 Establish Hybrid simulation code

The Hybrid kinetic-fluid method combines both methods of fluid and PIC. Here, ions are treated as super-particles, while electrons are treated as charge-neutralizing magneto fluid. Both schemes use the same spatial mesh and simulate on the same timestep.

The kinetic scales (cyclotron frequency, plasma frequency, Larmor radius, inertial length) of ions and electrons are what determine the appropriate model to use. The resistive fluid model employed here neglects heat flux and assumed the pressure is isotropic. It reduces the simulation time but requires particles to reach the thermal equilibrium and be dissipated by Coulomb collision. The hybrid model is necessary when the spatial dimension is larger than the electron

Larmor radius and ion inertial length, and the frequency is smaller than the proton cyclotron frequency.

The hybrid code employed in this dissertation work is inherited from the hybrid code developed by Liu (2007) and Min (2018) based on C++ as an implementation of the hybrid model (current advance method and cyclic leapfrog) described by Matthews (1994). The procedure of simulation is as follows. It begins with an initial ion velocity distribution at half-timestep $t^{n-1/2}$, where n is an integer, while the ion position and initial magnetic field are at t^n. Then, it calculates ion charge and current density at t^n. The electron pressure is then solved from ion charge density and fixed electron temperature at t^n. The electric field is then solved at t^n, but the contribution of electron resistivity is omitted in later calculations. After that, the system advances to next step, by first accelerating the ions from $t^{n-1/2}$ to $t^{n+1/2}$, then propagate ions from t^n to t^{n+1}. The ion charge and current density at $t^{n+1/2}$ are then calculated as an average. Then the electron pressure is solved at $t^{n+1/2}$. Then the magnetic field is propagated from t^n to t^{n+1}, which completes the loop. After that, the ion velocities at t^{n+1} are extrapolated from the half-timesteps for the need of analysis.

The hybrid model is adapted for parallel computing, by separating the space into many sub-domains and calculating the transport of the particles and fields between neighboring sub-domains. (For the case of the simulation code, it uses the Message Passing Interface (MPI) library to handle parallel computing). As communication efficiency only depends on the number of neighbors (or the spatial dimension), the total size of the system can be unlimitedly extended if there are enough computing nodes and processes. On the other hand, for a fixed size of a system, the number of processes has an upper limit, as the minimal cell size is limited by plasma wavelengths. The size of sub-domains and the computational power of processes should be balanced, as the total simulation time needed is decided by the slowest processes.

Chapter II. Simulation of continuously injected pickup ions

5. Background

The secondary ENA model and its variant described in Section 3.3, as the explanations of IBEX ribbon, raise the question of the stability of PUIs in a ring distribution outside the heliosphere. This part of the dissertation serves as an approach to that problem, which is described in our published paper (Sheng et al. 2021). This work was completed in part with resources provided by the Auburn University Easley Cluster.

There have been many studies addressing the stability of the PUI ring distribution. Florinski et al. (2010) used linear kinetic theory and 1D hybrid simulations to show that a ring distribution can be unstable to ion cyclotron waves, which leads to rapid (of the order of several days) cyclotron resonant scattering of the PUIs. Gamayunov et al. (2010) used quasilinear theory to calculate a pitch angle diffusion coefficient to address the scattering of the PUIs. Liu et al. (2012) performed 1D hybrid simulations and showed that once the density of the PUIs reached a certain level, the scattering times were short (on the order of 10 days) in agreement with the results of Florinski et al. (2010). Möbius et al. (2013) developed an analytic model of the secondary ENAs and concluded that the instabilities driven by the PUIs grow on a timescale of tens of days near the heliopause, not favoring the original secondary ENA explanation of the IBEX ribbon. Schwadron and McComas (2013) tried to reconcile the PUI stability challenge faced by the original secondary ENA mechanism by suggesting that strong scattering may produce a retention zone of the PUIs which supports the secondary ENA mechanism. Summerlin et al. (2014) used linear Vlasov analysis to show that if the ring-beam density is sufficiently small compared to the ambient plasma and if a realistic value for the temperature is used, the ring beam may be stable to parallel propagating ion cyclotron waves. Florinski et al (2016) used theoretical tools and 1D

hybrid simulations to study the kinetic behavior of PUIs with a ring distribution. They found that when the ring temperature is between 200 K and 30,000 K, there is a stability gap due to the damping of the Alfvén-ion cyclotron waves by the background plasma which has a Maxwellian distribution. Niemiec et al. (2016) used a 2D PIC code for the region outside the heliopause to confirm many of the features found in Florinski et al. (2016), but did not see the stability gap. This may be due to the scaled parameters used in the 2D PIC simulations. Min & Liu (2018) combined linear analysis and 2D hybrid simulations to show that mirror and ion Bernstein waves are unstable in the PUI ring distribution and can trigger the Alfvén cyclotron instability even if the distribution is initially in the stability gap. Zirnstein et al. (2020) used MHD along with a PUI transport equation in the weak scattering limit (Zirnstein et al., 2018) to show that the scale of turbulent fluctuations is important in determining whether secondary ENAs can explain the IBEX ribbon. Roytershteyn et al. (2019) performed 1D and 2D PIC simulations to investigate the stability of the PUIs and found instabilities due to fast growing quasi-parallel wave modes, but they found that these modes saturate at small amplitudes. More recently, Mousavi et al. (2020) performed linear instability analysis as well as 1D and 2D hybrid simulations for the same PUI distribution used in Roytershteyn et al. (2019). Their results demonstrated that obliquely propagating mirror modes are also unstable and contribute significantly to the scattering of the PUIs.

Clearly, which version of the secondary ENA mechanism is a viable explanation for the IBEX ribbon is not yet resolved. A key issue is the scattering of the initial ring distribution of the PUIs just outside the heliopause. In the study presented here, we use 2D hybrid simulations with continuous injection of PUIs perpendicular to the background magnetic field to study the PUI scattering. The background magnetic field strength, the energy of the PUIs, and the injection rate

are varied to provide new information regarding the two versions of the secondary ENA

mechanism for producing the IBEX ribbon.

6. Simulations

6.1 General method

The simulation results reported here provide new information regarding the secondary ENA explanation of the IBEX ribbon (McComas et al., 2009b, Schwadron and McComas, 2013). Protons which represent PUIs, are injected into a rectangular simulation box representing a region outside the heliopause. These PUIs are trapped by a static uniform external magnetic field representing the interstellar magnetic field and subsequently interact with the background plasma representing the LISM. The simulation determines the time evolution of the PUI velocity distribution which provides information for inferring the probability of a third charge exchange that creates an ENA contributing to the IBEX ribbon.

To provide a quantitative result as a solution to the problem, the physical parameters that bracket present observations are used to resolve the typical PUI scatter time (isotropization time, defined in Section 8.1) in the simulation. First, a representative case with the most probable parameters is investigated. The instabilities that occur in the system are specifically identified. Then, the evolutions and isotropization time are compared with other scenarios with varied PUI velocities and background magnetic field strength that cover the possible range in the outer heliosheath.

Due to limited computational power and simulation time, artificial PUI injection rates are used to speed up the simulation. Such rates are orders of magnitude higher than realistic values, which also changes the scattering time relative to the time when the PUI density reaches the same level. To examine the impact of this parameter, additional simulations with different injection rates are conducted. By extrapolating the logarithm of results linearly, the scattering time with a realistic PUI injection rate is estimated.

6.2 Simulation setting

A 2D hybrid model is used to simulate the collective behavior of the PUI's and LISM in the presence of the local ISMF. In a hybrid model, ions are treated as simulation particles, whereas the electrons are treated as a massless charge-neutralizing fluid. This model is appropriate for the study because the linear theory results of Min and Liu (2018) showed that the frequencies of the relevant instabilities are less than or of the same order as the proton cyclotron frequency. As in Liu et al. (2012), the charge exchange is implemented as a random process with LISM ions replaced by PUIs with a ring distribution with a finite thermal spread (see Equation (1) in Min and Liu, 2018). The number is set based on the input dimensionless PUI injection rate $\nu_{PUI} = (1/n_0\Omega_p)(dn_{PUI}/dt)$, where n_{PUI} represents the PUI density, n_0 is the LISM plasma density, $\Omega_p = eB_0/m_p$ is the proton cyclotron frequency, B_0 is the background magnetic field, and m_p is the proton mass.

A two-dimensional periodic rectangular simulation domain and three-dimensional velocity space (2D3V, the electric and magnetic fields vectors also have three dimensions) allow for the possible existence of the expected mirror mode instability and the development of Alfvén cyclotron waves and ion Bernstein waves. The x-axis and y-axis are sides of rectangular. The background magnetic field B_0 lies along the x-axis. The spatial sizes of the simulation cells are chosen to be $\Delta x = 1.4\ \lambda_p$ and $\Delta y = 2.8\ \lambda_p$, where $\lambda_p = \sqrt{(m_p/\mu_0 n_0 e^2)}$ is the proton inertial length of the background plasma. The numbers of cells are chosen to be $Nx = 960$ and $Ny = 480$ to accommodate the expected wavelengths of the mirror mode and ion Bernstein waves according to the linear analysis of Min and Liu (2018). The initial number of LISM particles per cell is set at 1000, and it will decrease with the evolution of time. The simulation time step is $\Delta t\Omega_p = 0.01$.

As the injected PUIs have a low density compared to LISM, each simulated PUI particle represents a number density as 1/50 of a LISM particle. Therefore, when 50 new PUI particles are injected into the system, 1 random LISM particle of size 50 times large is removed from the system. The continuous charge exchange occurs as repeated charge exchange processes with time interval set at $\tau\Omega_p = 2.5$. The numerical resistivity, which determines the magnetic diffusion term, is set as a small value of $\eta = 9\times10^{-5}$.

The simulation uses dimensionless parameters. The magnetic field fluctuations are scaled in terms of the background magnetic field B_0. Velocities are scaled in terms of the Alfvén speed $v_A = B_0/\sqrt{(\mu_0 n_0 m_p)}$. Distance is scaled in terms of the proton inertial length λ_p. The ions are all protons. Time is scaled in terms of the inverse of the ion cyclotron frequency $(\Omega_p)^{-1}$.

6.3 Physical parameters

The physical parameters that determine the dimensionless parameters are chosen to represent the environment of the region just outside the heliopause. The background plasma density $n_0 = 0.1$ cm^{-3}. Three values for the background magnetic field $B_0 = 0.3, 0.5,$ and 0.7 nT are chosen to span the range of the measurements from Voyager 1 and 2 (Gurnett et al. 2013 & Burlaga 2019). This gives $\lambda_p = 720$ km, $v_A = 20.7, 34.5, 48.3$ km/s and $\Omega_p = 0.0287, 0.0479, 0.0671$ s^{-1} respectively (See Table 1). The initial temperature of the background plasma is $T_0 = T_e = 40{,}000$ K, which gives $\beta = 1.442, 0.558, 0.284$, respectively ($\beta = n_0 k_B T_0/(B_0^2/2\mu_0)$). This temperature is in the middle of the range of the Voyager 2 data $T_0 = 30{,}000 \sim 50{,}000$ K (Richardson 2019). The perpendicular, $T_{\perp r}$, and parallel, $T_{\parallel r}$, ring temperatures of the PUIs that give the initial thermal spread of the PUI ring distribution (See Equation (2) and text below in Min and Liu, 2018) are 100,000 K. The initial bulk speed of the LISM is set to $v_{LISM} = 0$ as the reference frame. The ring

speed of the injected PUIs is v_{PUI}= 400, 600, 800 km/s, with the corresponding kinetic energies

0.835, 1.88, 3.34 keV, which spans the range of the energy of the IBEX ribbon (McComas et al.

2014).

Parameter	Unit of	Formula	Value		
Magnetic field strength		B_0	0.3 nT	0.5 nT	0.7 nT
Ion inertial length	Distance	λ_p	720 km	720 km	720 km
System size (square)		1344 Ω_p	0.0065AU	0.0065AU	0.0065AU
Ion cyclotron frequency		Ω_p	0.0287 s^{-1}	0.0479 s^{-1}	0.0671 s^{-1}
Ion cyclotron period	Time	1/ Ω_p	34.8 s	20.9 s	14.9 s
Alfvén speed	Speed	v_A	20.7 km/s	34.5 km/s	48.3 km/s
Magnetic field energy	Energy	B_0^2/μ_0	71.6 pJ	199 pJ	390 pJ

Table 1. The physical parameters in the simulation.

The initial pitch angle (the angle between the particle's velocity vector and the local magnetic

field) of the injected PUIs is around 90°. This means that the simulated region is where the

magnetic field **B$_0$** is perpendicular to the velocity direction of the solar wind **v$_{SW}$** as well as to the

line of sight to IBEX **r**. This setting is a representation of the heliosheath region in the center of

IBEX ribbon direction by ignoring the small variance (<10°) of the angle between **B$_0$** and **r** or

the width of the ribbon (See Figure 15).

Note that it is not difficult to adjust the initial pitch angle of PUIs. However, that is not enough to

simulate regions outside the ribbon direction. Because the difference between the average pitch

angle and 90° determines the drift motion of particles parallel to the magnetic field. The PUIs in

the region outside but close to the ribbon direction have initial pitch angles near 90° and the PUIs

in the region far from the ribbon direction have initial pitch angles much larger or smaller than

90°, and all make them drift away from the ribbon direction considering the radius direction and

the curvature of the magnetic field line. On the other hand, the scattering of the PUI will change

the pitch angle as well as the drift motion. When the number of particles moving out and into the

simulated region has a significant difference, there will be a transport effect that cannot be

ignored. Thus, there will be multiple kinds of PUIs in the region outside the ribbon direction. One is the injected PUIs that come from the sun direction with fixed initial pitch angle θ, and the others are the transported PUIs with various pitch angles, which travel from neighboring regions in the heliosheath along the magnetic field lines. These transported PUIs are both the reason for and the result of PUI scattering, so a global simulation along the field line is needed to provide the complete picture instead of the local simulation reported here.

7. Results

7.1 Representative case

In this section, we present results from the simulations, which include the time evolution of the thermal energy and the wave flow energies (the kinetic energies of wave-related fluid flows) in the PUIs and the background plasma, and the wave magnetic and electric field energies. The spatial distribution along with the wavenumber power spectrum of the magnetic field fluctuations are shown for times of interest. The latter helps identify the wave modes. The effects of varying the strength of the background magnetic field, B_0, the ring velocity of the PUIs, v_{PUI}, and the PUI injection rate (in s^{-1}), $v_{PUI}\Omega_p$, are then described.

We first show the results for a representative case, i.e., $B_0 = 0.5$ nT, $v_{PUI} = 600$ km/s, and $v_{PUI}\Omega_p = 1.9 \times 10^{-7}$ s^{-1} (so $v_{PUI} = 4 \times 10^{-6}$). Figure 16 shows the various energies as a function of time. A key feature is the transition from a mirror mode dominated phase to an Alfvén ion cyclotron wave dominated phase at about $t\Omega_p = 400$. In Figure 16(a), we see that the thermal energy of the PUIs grows mostly linearly due to the constant injection rate. Initially, it is the thermal energies in the perpendicular, y and z, directions that grow followed by growth primarily in the parallel, x, direction. We will see in the next figure that this is due to a transition from the mirror mode to the Alfvén ion cyclotron wave dominating the physical development.
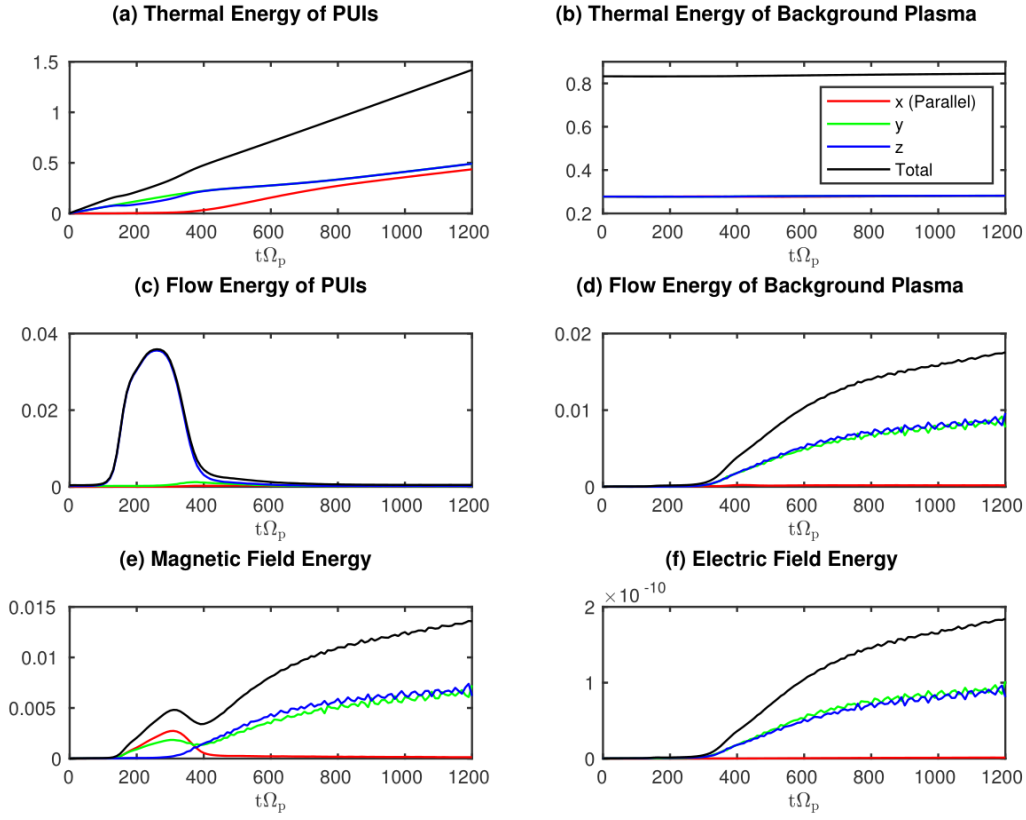
Figure 16. Time evolution of (a) PUI thermal energy, (b) background plasma thermal energy, (c) PUI bulk flow energy, (d) background plasma bulk flow energy, (e) magnetic field energy, and (f) electric field energy, in units of B_0^2/μ_0, with the same color scheme as showed in panel (b), for representative values $B_0 = 0.5$ nT, $v_{PUI} = 600$ km/s, and $v_{PUI}\Omega_p = 1.9\times10^{-7}s^{-1}$.

Note that Figure 16(a) shows that as time grows, the thermal energy of the PUI ions in the x, y, and z directions become equal, i.e., the distribution becomes isotropic. Figure 16(b) shows that the thermal energy of the background plasma remains approximately constant. In Figure 16(c), the wave flow energy in the PUIs peaks in the early time period, and the wave flow energy of the background plasma, Figure 16(d), grows during the second time period. The bulk plasma flow associated with the mirror mode is mainly in the PUIs, while it is mainly in the background ions

40

for the Alfvén ion cyclotron waves developed later. Note that the wave flow energies are small compared to the thermal energies. In Figure 16(e), the energy in the magnetic field fluctuations is initially due to the mirror mode waves carried by PUIs with peaks in the parallel, x, and perpendicular, y, direction. This is followed by a growth in the perpendicular, y and z, directions while the parallel fluctuations decay to 0 during the time period dominated by Alfvén ion cyclotron waves that propagate in the background plasma. The energy in the electric field fluctuations, see Figure 16(f), is very small throughout the time interval, becoming nonzero only during the period dominated by the Alfvén ion cyclotron waves. Note the out of phase small energy variations in both the perpendicular magnetic and electric field fluctuations during the second period (see Figures 16(e) and 16(f)).

Figure 17 presents the y component of the magnetic field (left column), which is nonzero for both the mirror and ion cyclotron modes, and the corresponding wavenumber power spectra (right column) at selected times for the representative case. In the left column, the oblique fluctuations 45° from x-axis strengthen in the early times (see Figures 17(a) and 17(c)), peaking at $t\Omega_p \approx 300$ (See Figure 16(e)). The waves are propagating at approximately 45 degrees. Subsequently the waves continue to strengthen but become parallel propagating (see Figures 17(e) and 17(g)). In the right column, the wavenumber spectra clearly show the transition from the mirror mode to the Alfvén ion cyclotron mode. The modes are identified from the linear analysis in Min and Liu (2018). In Figures 17(b) and 17(d), the dominant waves are at large wavelengths with k_x and k_y approximately equal. These are mirror mode. As time progresses, the dominant waves have k_x much larger than k_y, which are identified as quasi-parallel Alfvén ion cyclotron waves. The strength of the mirror mode declines.
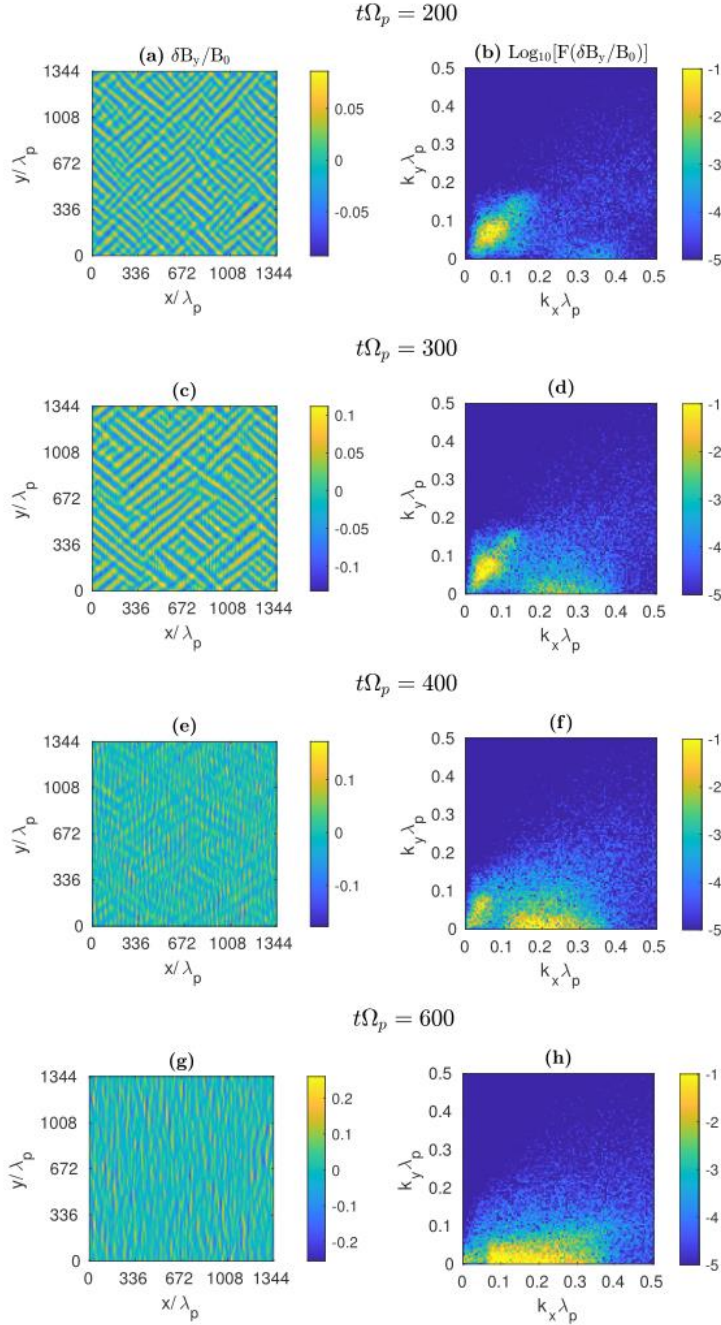
Figure 17. The spatial form of the y component of the magnetic field fluctuations (left column) and the logarithm of the corresponding wave number power spectra (right column) as a function of k_x and k_y for $t\Omega_p = 200, 300, 400, 600$, with the same parameters as Figure 16.

Figure 18 shows the time evolution of the PUI velocity distribution for the representative case. We see that at the initial time, the distribution is a ring with a small thermal spread determined

by the initial temperature of the PUIs. During the time period that the mirror mode is dominant, Figures 18(a-c), the PUI distribution broadens mostly in the parallel direction, becomes a partial-shell distribution. When the Alfvén ion cyclotron waves dominate, Figures 18(d-f), the scattering is also primarily in the parallel direction but becomes stronger. By the time $t\Omega_p = 900$, the distribution is nearly isotropic, as a spherical shell distribution. The significance of this scattering time with respect to the viability of the secondary ENA mechanism is discussed in Section 8.
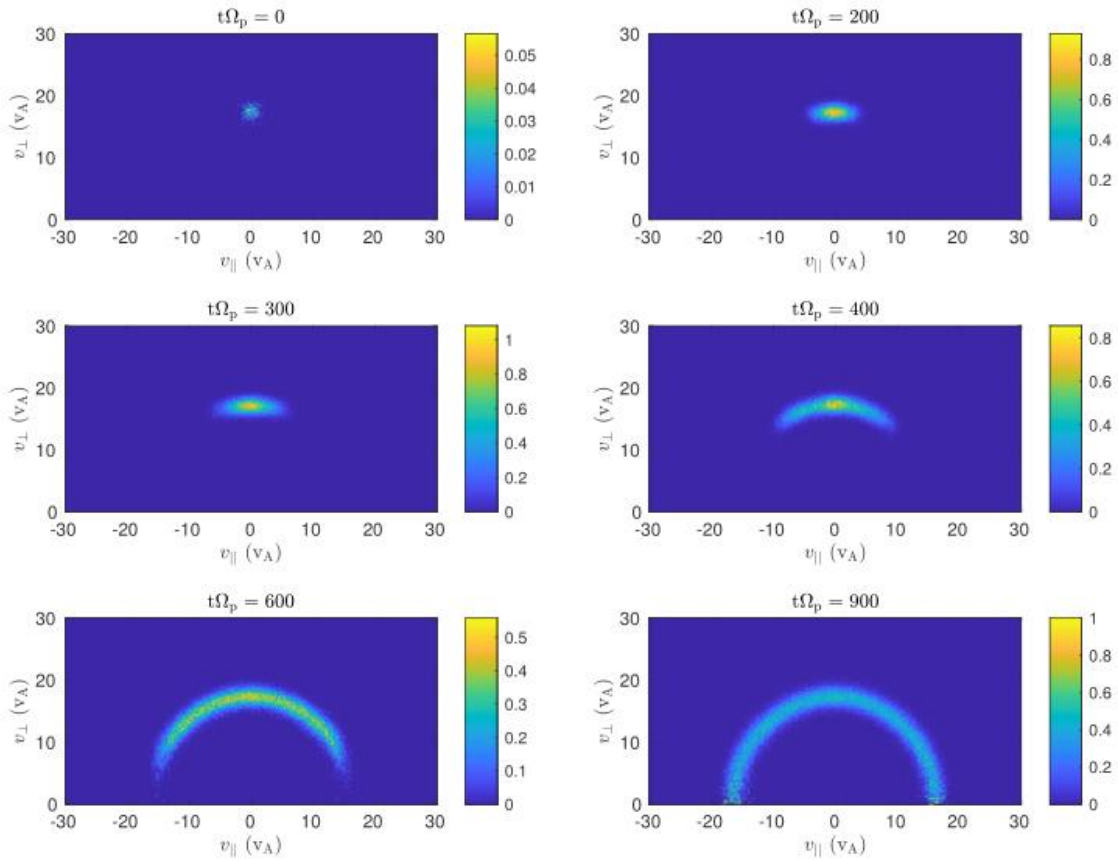
Figure 18: Graphs of the velocity distributions of the PUIs in terms of perpendicular and parallel velocities, in units of v_A, when $t\Omega_p = 0, 200, 300, 400, 600, 900$, with the same parameters as Figure 16.

The specific beta β_s of a plasma species s, defined as the ratio of its thermal pressure $p_s = n_s k_B T_s$ to the magnetic pressure $p_m = B_0^2/(2\mu_0) = (1/2) n_0 m_p v_A^2$, is an important parameter in the study

plasma instabilities related to the species. For PUIs with anisotropic and non-Maxwellian velocities distribution, the uniform thermal pressure and temperature are not well defined, but we can still calculate the ion pressure on each coordinate, e.g., $p_{PUI,x} = n_{PUI}m_p\langle v_{PUI,x}^2\rangle$, two times of the x component of the thermal energy of PUIs. So that, we could define p_{PUI} as the mean ion pressures on x, y and z directions, and the parallel pressure defined as the mean ion pressures on y and z directions. Therefore, we can define $\beta_{PUI} = (n_{PUI}/n_0)((2/3)\langle v_{PUI}\rangle^2/v_A^2)$. Similarly, we can define $\beta_{PUI,\parallel}$ and $\beta_{PUI,\perp}$ (see Figure 19).
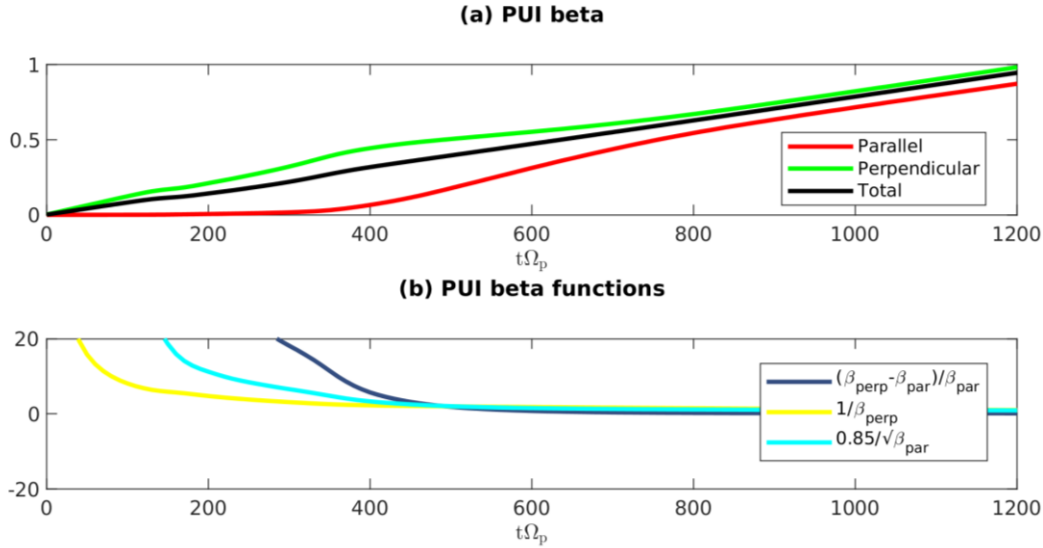
Figure 19. Time evolution of (a) PUI beta, red line is $\beta_{PUI,\parallel}$, green line is $\beta_{PUI,\perp}$, black line is β_{PUI}, (b) some functions for PUI beta that related to MHD threshold of mirror mode and Alfvén ion cyclotron waves, which all intersect at $t\Omega_p \sim 500$, for representative values $B_0 = 0.5$ nT, $v_{PUI} = 600$ km/s, and $v_{PUI}\Omega_p = 1.9\times10^{-7}$s^{-1}.

As the PUIs are injected into the system, the PUI density increases and thus its contribution to the ion pressure increases linearly, while the ion pressure of background plasma p_0 and the magnetic pressure remain the same ($\beta_{BG} = \beta_0 = 0.558$). So, the total plasma beta $\beta = \beta_{BG} + \beta_{PUI}$ is increased. With the ring speed $v_{PUI} = 17.4\ v_A$, much larger than the thermal spread of background

plasma $\theta_{BG} = 0.745$ v_A, a small amount of PUIs makes a significant contribution to the total

plasma β. Note, the largest contribution to β_{PUI} comes from the ring speed of the PUIs, not the

thermal spread of the ring distribution, $\theta_{ring,\parallel} = \theta_{ring,\perp} = 1.18$ v_A. In the early stage of the

simulation, $\beta_{PUI,\perp}$ is significantly larger than $\beta_{PUI,\parallel}$, until the PUI velocity distribution is scattered.

At $t\Omega_p = 400$, when the phase transition occurred, $\beta_{PUI,\parallel} = 0.04$, $\beta_{PUI,\perp} = 0.29$ and $\beta_{PUI} = 0.33$, the

total plasma $\beta = 0.89$. The total plasma β is not exceeding 1, until $t\Omega_p \sim 550$.

7.2 Varying PUI velocities and Background magnetic field Strength

The qualitative characteristics of the wave development and the isotropization of the PUIs

remain the same as we vary the background magnetic field, the PUI ring velocity, and the PUI

injection rate. For the parameters used in the simulations presented here, there are no indications

of significant ion Bernstein waves, which is consistent with the linear growth rates in Min and

Liu (2018), i.e., the linear growth rates of the mirror mode are larger than those for the ion

Bernstein waves for the larger beta values of the background plasma and the PUI ring beta.

Figure 19 shows the time evolution of the energy of the magnetic field fluctuations for $B_0 = 0.3$,

0.5, 0.7 nT and for $v_{PUI} = 400$, 600, 800 km/s, while the dimensionless PUI injection rate v_{PUI} is

scaled by 0.5 nT/B_0, to keep the PUI injection rate (in s^{-1}) $v_{PUI}\Omega_p$ the same as the representative

case, so that $v_{PUI}\Omega_p = 1.9\times10^{-7}$ s^{-1}. We see that as B_0 increases at fixed v_{PUI}, the mirror mode

weakens. On the other hand, as v_{PUI} increases for fixed B_0, the energy in the magnetic field

fluctuations increases. These trends are indeed consistent with the linear analysis in Min and Liu

(2018) that shows the mirror instability growth rate increases more dramatically than the Alfvén

cyclotron instability (and the ion Bernstein instability) with the increase of the ring speed (in

terms of v_A) and, therefore, should become more pronounced when the ring speed is larger or B_0

is smaller. The other basic characteristics of the time evolution of the magnetic fluctuations, however, remain very similar.

Porazik & Johnson (2013), using gyrokinetic simulations of the evolution of mirror mode waves found saturation due to the development of trapping regions as a result of field line tension. The magnetic field perturbations in our Figures 17(a) and 17(c) resemble the configuration from the end of their simulation in their Figure 5. Examining the evolution of the energy in the magnetic field fluctuations for a range of parameters in Figure 20, we see growth and then perhaps levelling off and finally decay during the time period of strong mirror mode waves. For times longer than those considered by Porazik & Johnson (2013), we see growth of Alfvén ion cyclotron waves and stronger growth in the energy of the magnetic fluctuations. The effect on the stability of the initial PUI ring distribution will be discussed in Section 8.
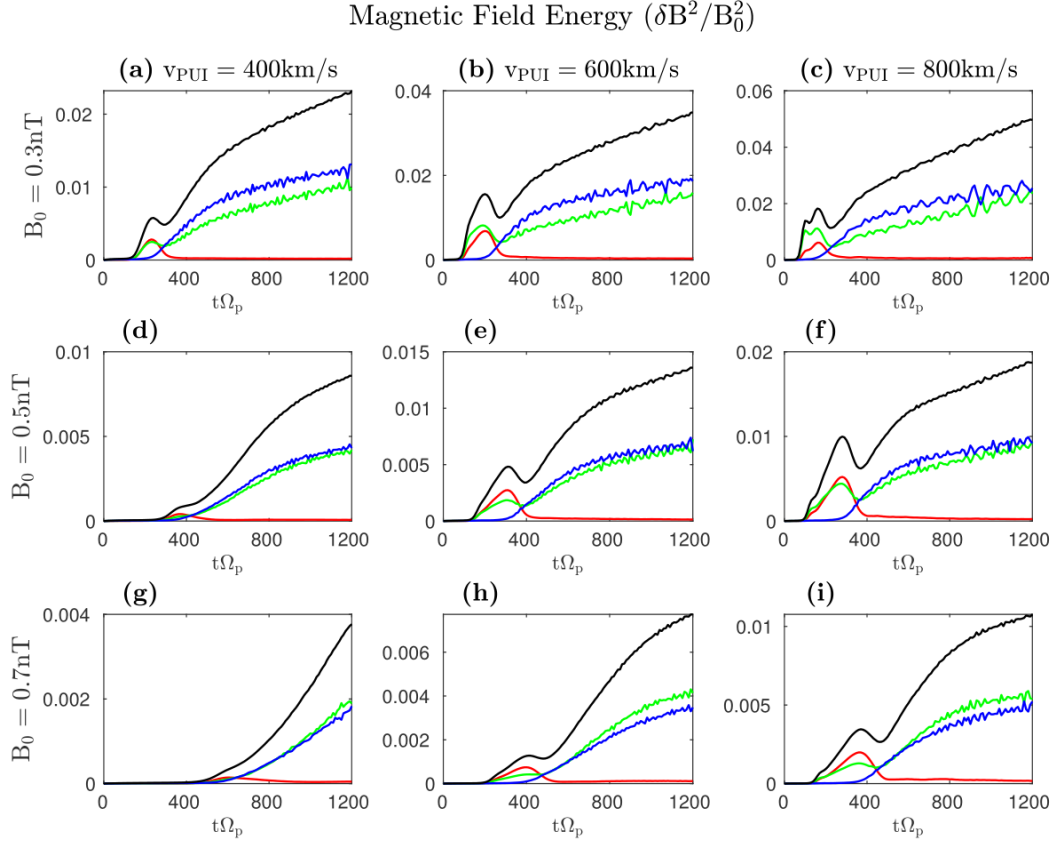
Magnetic Field Energy $(\delta B^2/B_0^2)$

Figure 20. The time dependence of the magnetic field energy for $B_0 = 0.3, 0.5, 0.7$ nT and $v_{PUI} = 400, 600, 800$ km/s with $v_{PUI}\Omega_p = 1.9\times10^{-7}$ s^{-1}.

8. Discussion and Conclusions

8.1 PUI injection rate

We have presented results from 2D space, 3D velocity hybrid simulations of the plasma processes that are responsible for pitch angle scattering of the PUIs in the outer heliosheath. While we see evidence for the prominent physical processes seen in previous simulations, there are important differences.

The parameters considered in the simulations here span values thought to be relevant to the region just outside the heliopause where the secondary ENAs can contribute to the IBEX ribbon. We see a mix of mirror modes and Alfvén ion cyclotron waves. It is the Alfvén ion cyclotron waves that are the primary scatterers producing the isotropization of the PUI ring distribution. It is the time required for the scattering of the PUIs into the direction parallel to the ambient magnetic field that is crucial to determining whether one of the two versions of the secondary ENA mechanism is a viable explanation for the IBEX ribbon.

We will use $T_\parallel/T_\perp$, i.e., the ratio of the parallel to perpendicular PUI thermal energy, as a measure of the degree of isotropization. It is difficult to define a precise value at which this ratio is too large, i.e., at what value the initial ring becomes a wide shell-like pitch angle distribution so that the PUIs do not contribute to the IBEX ribbon via the original version of the secondary ENA mechanism. Möbius et al. (2013) showed that a narrow velocity ring distribution may provide an even higher ENA flux than observed. Liu et al. (2012) chose a value of $<\Delta\alpha^2> = 0.2$ as a measure of the degree to which the PUIs are significantly scattered, where $\Delta\alpha^2$ is the variance of pitch angle and $<...>$ represents averaging over all PUIs. Looking at our Figure 21(b), we see that for the representative case we have illustrated in detail $T_\parallel/T_\perp$ reaches a value of 0.15 at $t = 8352$ s or $t\Omega_p = 400$. Looking at the pitch angle distributions in Figures 18(c) and

48

18(d), when $t\Omega_p$ is between 300 and 400, it seems reasonable to define an isotropization time, τ_{iso}, as the time at which $T_\parallel/T_\perp$ is near 0.15.

Figure 21 shows the time dependence of $T_\parallel/T_\perp$ for the range of background magnetic field strengths and PUI ring velocities shown in Figure 19. We plot here in units of seconds rather than the dimensionless units of the simulation time. We see in each frame that as the ring velocity of the PUIs increases from 400 km/s to 800 km/s, τ_{iso} decreases. As the strength of the magnetic field increases from 0.3 nT to 0.7 nT, τ_{iso} increases for a fixed value of the PUI velocity. The span is from 5220 s for $B_0 = 0.3$ nT and $v_{PUI} = 400$ km/s to 12,229 s when $B_0 = 0.7$ nT and $v_{PUI} = 800$ km/s, i.e., about a factor of 2. It is to be noted that the injection rate (in s^{-1}) is the same, i.e., $v_{PUI}\Omega_p = 1.9\times10^{-7}$ s^{-1}.

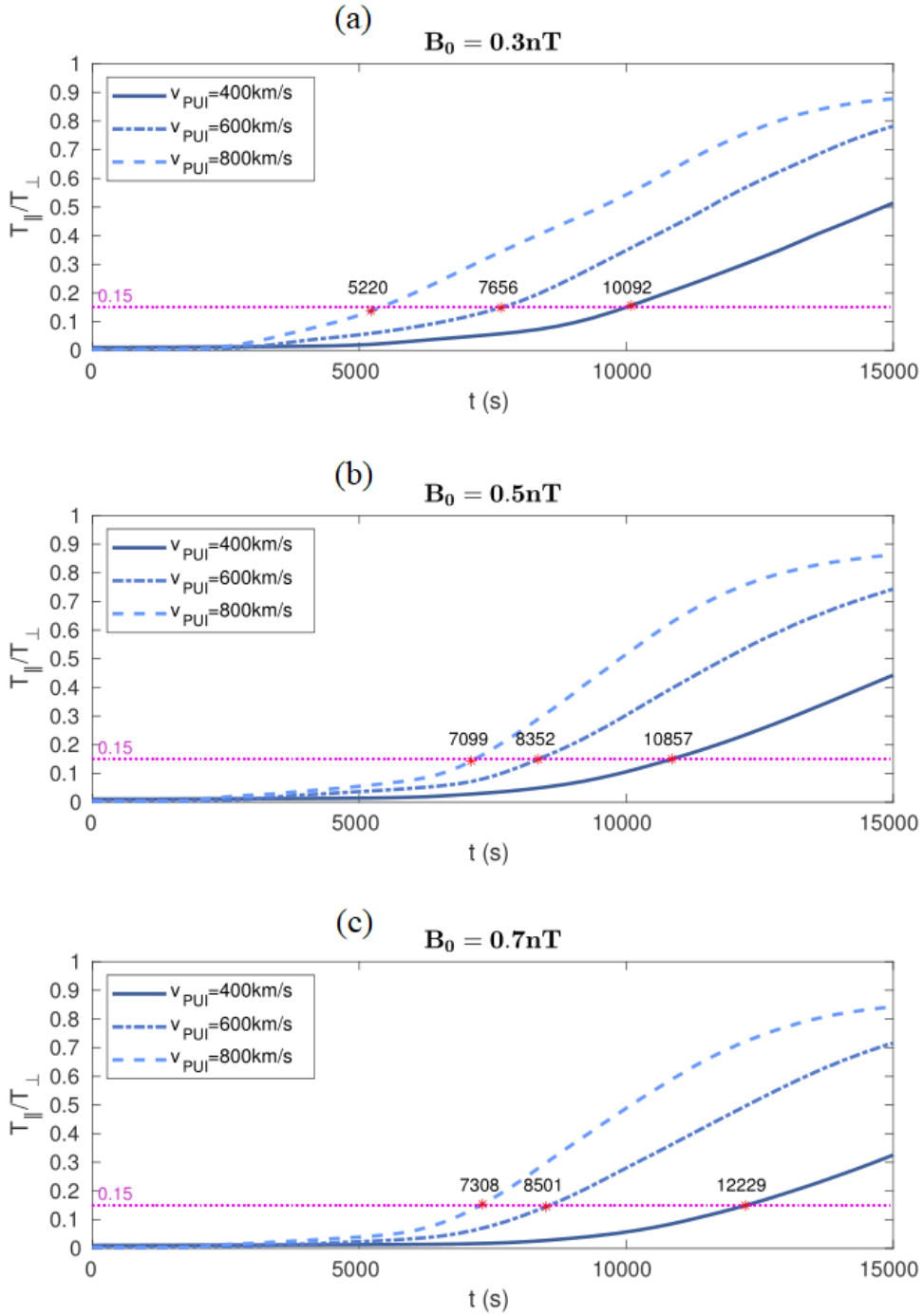**Figure 21.** The time dependence in seconds of $T_\parallel/T_\perp$ for $B_0 = 0.3, 0.5, 0.7$ nT and $v_{PUI} = 400$, 600, 800 km/s with $v_{PUI}\Omega_p = 1.9\times10^{-7}$ s^{-1}, the threshold 0.15 and the time each simulation reach the threshold are marked.

The key reason for this result might be the relative strength between ion thermal pressure and magnetic pressure, as increasing of the ring velocity increases the ion pressure, and the decreasing of B_0 decrease the magnetic pressure, all contribute to a large beta, and flavor the growth of Alfvén ion cyclotron instability (Though, no certain threshold of beta can be given for this non-linear problem). The result of velocities dependence shows the same trend of IBEX image with different energies. The result of magnetic dependence narrowed the possible source region of ENA (see Figure 15).

The new feature of the simulations presented here is the continuous injection of the PUIs, with the injection rate, $\nu_{PUI}\,\Omega_p$. By calculating the charge exchanging rate use the charge-exchange cross section, a realistic value is given by $\nu_{PUI}\Omega_p = n_{NSW} \cdot \sigma_{exc} \cdot v_{NSW} = 1.36 \times 10^{-12}\,s^{-1}$ or $\nu_{PUI} = 2.0 \times 10^{-11}$ to 4.7×10^{-11}, i.e., for B_0 from 0.3 to 0.7 nT, where $n_{NSW} = 2 \times 10^{-5}\,cm^{-3}$ is a typical solar wind neutral density at the heliopause, $\sigma_{exc} = 1.7 \times 10^{-15}\,cm^2$ is the charge exchange cross section at 1 keV (Zank, 1999), and $v_{NSW} = v_{PUI} = 400$ km/s is a typical solar wind neutral velocity. As pointed out by Liu et al. (2012), simulations with a realistic rate of this order of magnitude require too much computer time. Liu et al. (2012) performed their 1D simulations with injection rates covering a range from 10^{-5} to 10^{-9}. They found that the logarithm of a scattering time calculated during the time of the linear growth phase of the waves varied linearly with the logarithm of the injection rate.

We have performed the 2D simulations varying the PUI injection rate from $\nu_{PUI}\Omega_p = 1.9 \times 10^{-7}\,s^{-1}$ to $3.0 \times 10^{-9}\,s^{-1}$. Figure 22 shows values of τ_{iso} for five values of the injection rate. Here $B_0 = 0.5$ nT, $v_{PUI} = 600$ km/s, the same parameters used in Figures 16~18. Times measured in seconds for $T_\parallel/T_\perp = 0.1$, 0.15, and 0.2 are marked. As expected, τ_{iso} increases with the decrease in the injection rate. Similar to the results of Liu et al. (2012) for 1D simulations, the dependence is nearly linear in logarithmic scales. Extrapolating to realistic values of the injection rate, $\nu_{PUI}\Omega_p =$

10^{-12} s^{-1}, gives τ_{iso} time between 0.1 to 0.2 yr. These times will vary somewhat depending on the strength of the magnetic field and the PUI ring velocity by 0.6~1.5 times as shown in Figure 21. It is also to be noted that this is an extrapolation over a long range. Nevertheless, the time for the stability of the injected PUI distribution just outside the heliopause in the ribbon direction sheds light on the viability of the two versions of the secondary ENA mechanism as a major contributor to the IBEX ribbon.
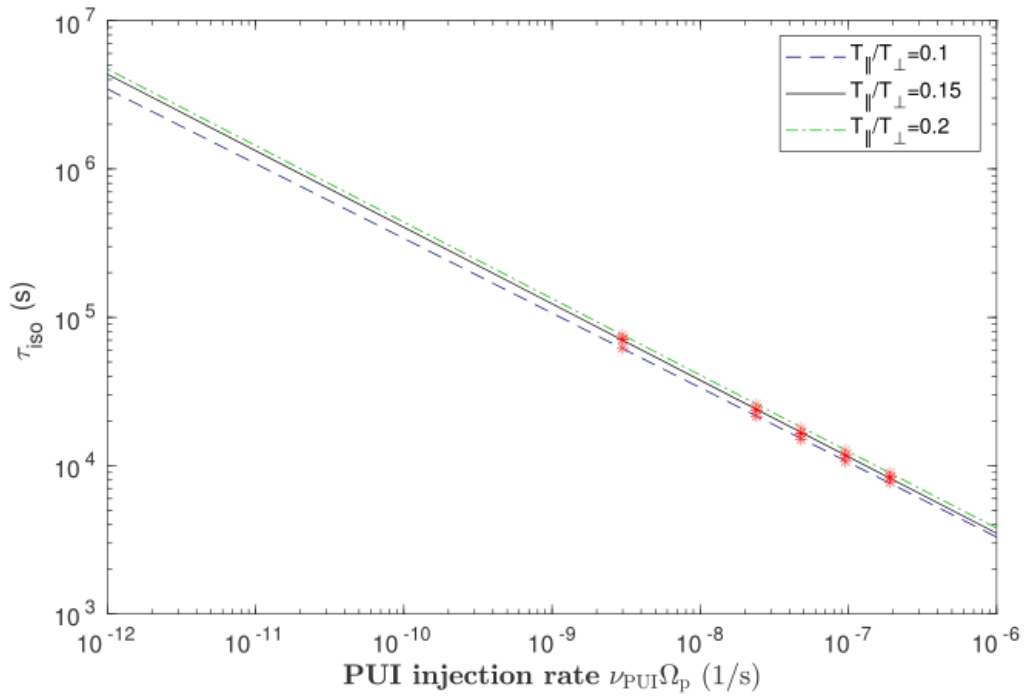

Figure 22. Extrapolation of τ_{iso} as a function of the PUI injection rate $\nu_{PUI}\Omega_p$ in units of inverse seconds.

8.2 Conclusion for Secondary ENA model

The original version of the secondary ENA mechanism, proposed by McComas et al. (2009b) and modeled by Heerikhuisen et al. (2010), Chalov et al. (2010), Möbius et al. (2013) and Zirnstein et al. (2016, 2018), requires weak scattering of the PUIs in all regions. The ring-beam distribution of PUIs in the outer heliosheath needs to be stable over years, before they charge exchange with the interstellar neutrals and convert into ENAs that would contribute to the IBEX ribbon (e.g.,τ_{ex} ~ 6×10^7 s ~ 2 yr; Heerikhuisen et al., 2010). Since the parallel velocities of the secondary ENAs remain the same as the PUIs from which they are converted, only the ENAs with pitch angles of ~90±10° in the ribbon direction can return to the Sun and be observed by IBEX producing the observed ribbon structure alignment with the $\mathbf{B}\cdot\mathbf{r}$ ~ 0 surface, where $\mathbf{r}$ is the radial line of sight. The short isotropization time estimated here poses a challenge to this version of the secondary ENA mechanism. The isotropization time, τ_{iso} ~ 0.1 to 0.2 yr, is an order of magnitude too small. The scattering is too strong and would result in a weaker and broader ribbon than observed by IBEX.

In contrast to the original version of the secondary ENA mechanism that requires the long-term stability of the PUIs in the ribbon direction, Schwadron and McComas (2013) presented an alternative version of the secondary ENA mechanism that instead needs strong scattering of the PUIs in the ribbon direction. They argued that strong scattering can lead to spatial retention of the PUIs in the ribbon direction, while the PUIs in other directions are injected with substantial initial velocities parallel to the background interstellar magnetic field and thus stream away from the retention region. This explains the narrow ENA ribbon observed. Subsequently, Isenberg (2014) developed a physically motivated, quantitative mechanism to produce the spatial retention based upon an assumption of "dominant turbulence". Additionally, Giacalone and Jokipii (2015)

presented a model in which fluctuations of the magnetic field in the local interstellar medium create a region of enhanced PUI density due to magnetic mirroring.

The simulation results reported here confirm the strong scattering in the ribbon direction by considering the effects of continuous injection of PUIs perpendicular to the interstellar magnetic field. The study does not yet address the strength of the scattering outside the "retention region." So, while the strong scattering supports the alternative version of the secondary ENA mechanism, final confirmation requires additional studies of the PUI stability in the off-ribbon directions and more detailed calculations of the transport effect of PUIs and the ENA flux to be observed by IBEX. This is beyond the scope of this investigation. The isotropization time found in this study is, however, too short ($\approx 0.1 \sim 0.2$ yr) for the original version of the PUI explanation for the IBEX ribbon.

8.3 Conclusion

In order to verify the secondary ENA models, we have used 2D hybrid simulation with continuous PUI injection to find out its isotropization time in the center region of ribbon direction. The result shows longer time of scattering of PUI velocity distribution than previous studies but still too short for original version of secondary ENA models. Further study, such as global simulation of heliopause with variation of pitch angle of the injected PUI and the effect of PUI transport alone the magnetic field line is needed for the second version of secondary ENA models that predicts ion retention region. Variation of the injection rate might also be critical to simulate the full solar cycle variance of the ribbon.

Reference

Burlaga, L. F., Ness, N. F., Berdichevsky, D. B., et al. (2019). Magnetic field and particle measurements made by Voyager 2 at and near the heliopause. *Nature Astronomy*, 3, 1007–12. https://doi.org/10.1038/s41550-019-0920-y

Chalov, S. V., Alexashov, D. B., McComas, D. J., et al. (2010). Scatter-free Pickup Ions beyond the Heliopause as a Model for the Interstellar Boundary Explorer Ribbon. *The Astrophysical Journal Letters*, 716, L99. https://doi.org/10.1088/2041-8205/716/2/L99

Dayeh, M. A., Zirnstein, E. J., Desai, M. I., et al. (2019). Variability in the Position of the IBEX Ribbon over Nine Years: More Observational Evidence for a Secondary ENA Source. *The Astrophysical Journal*, 879, 84. https://doi.org/10.3847/1538-4357/ab21c1

Dryer, M. (1987). Solar Wind and Heliosphere, in: "The Solar Wind and the Earth", S.-I. Akasofu and Y. Kamide, eds., Terra Scientific Publishing Company, Tokyo.

Ferrière, K. (2001). The Interstellar Environment of our Galaxy. *Reviews of Modern Physics*, 73(10), 1103. https://doi.org/10.1103/RevModPhys.73.1031

Ferrière, K. (2009). Interstellar magnetic fields in the Galactic center region. *Astronomy & Astrophysics*, 505(3), 1183-1198. https://doi.org/10.1051/0004-6361/200912617

Florinski, V., Zank, G. P., Heerikhuisen, J., et al. (2010). STABILITY OF A PICKUP ION RING-BEAM POPULATION IN THE OUTER HELIOSHEATH: IMPLICATIONS FOR THE IBEX RIBBON. *The Astrophysical Journal*, 719, 1097. https://doi.org/10.1088/0004-637X/719/2/1097

Florinski, V., Heerikhuisen, J., Niemiec, J., & Ernst, A. (2016). THE IBEX RIBBON AND THE

PICKUP ION RING STABILITY IN THE OUTER HELIOSHEATH. I. THEORY AND

HYBRID SIMULATIONS. *The Astrophysical Journal*, 826, 197. https://doi.org/10.3847/0004-

637X/826/2/197

Frisch, P. C., Andersson B-G, Berdyugin A., et al. (2012). THE INTERSTELLAR MAGNETIC

FIELD CLOSE TO THE SUN. II. *The Astrophysical Journal*, 760, 106.

https://doi.org/10.1088/0004-637x/760/2/106

Funsten, H. O., Allegrini, F., Bochsler, P., et al. (2009a). The Interstellar Boundary Explorer

High Energy (IBEX-Hi) Neutral Atom Imager. *Space Science Reviews*,146, 75.

https://doi.org/10.1007/s11214-009-9504-y

Funsten, H. O., Allegrini, F., Crew, G. B., et al. (2009b). Structures and Spectral Variations of

the Outer Heliosphere in IBEX Energetic Neutral Atom Maps. *Science*, 326, 964.

https://doi.org/10.1126/science.1180927

Fuselier, S. A., Allegrini, F., Funsten, H. O., et al. (2009). Width and Variation of the ENA Flux

Ribbon Observed by the Interstellar Boundary Explorer. *Science*, 326, 962.

https://doi.org/10.1126/science.1180981

Gloeckler G. & Geiss J. (1998). Interstellar and Inner Source Pickup Ions Observed with Swics

on Ulysses. *Space Science Reviews*, 86, 127. https://doi.org/10.1023/A:1005019628054

Gamayunov, K., Zhang, M., & Rassoul, H. (2010). PITCH ANGLE SCATTERING IN THE

OUTER HELIOSHEATH AND FORMATION OF THE INTERSTELLAR BOUNDARY

EXPLORER RIBBON. *The Astrophysical Journal*, 725, 2251. https://doi.org/10.1088/0004-

637X/725/2/2251

Giacalone, J., & Jokipii, J. R. (2015). A NEW MODEL FOR THE HELIOSPHERE'S "IBEX

RIBBON". *The Astrophysical Journal Letters*, 812, L9. https://doi.org/10.1088/2041-
8205/812/1/L9

Gurnett, D. A., Kurth, W. S., Burlaga, L. F., & Ness, N. (2013). In situ observations of

interstellar plasma with Voyager 1. *Science*, 341, 1489. https://doi.org/10.1126/science.1241681

Heerikhuisen, J., Pogorelov, N. V., Zank, G. P., et al. (2010). PICK-UP IONS IN THE OUTER

HELIOSHEATH: A POSSIBLE MECHANISM FOR THE INTERSTELLAR BOUNDARY

EXplorer RIBBON. *The Astrophysical Journal*, 708, L126. https://doi.org/10.1088/2041-
8205/708/2/L126

Isenberg, P. A. (2014). SPATIAL CONFINEMENT OF THE IBEX RIBBON: A DOMINANT

TURBULENCE MECHANISM. *The Astrophysical Journal*, 787, 76.

https://doi.org/10.1088/0004-637X/787/1/76

Liu, K., Möbius, E., Gary, S. P., & Winske, D. (2012). Pickup proton instabilities and scattering

in the distant solar wind and the outer heliosheath: Hybrid simulations. *Journal of Geophysical

Research*, 117, A10102. https://doi.org/10.1029/2012JA017969

Matthews, A. P. (1994). Current Advance Method and Cyclic Leapfrog for 2D Multispecies

Hybrid Plasma Simulations. *Journal of Computational Physics*, 112, 102.

https://doi.org/10.1006/jcph.1994.1084

McComas, D. J., Allegrini, F., Bochsler, P., et al. (2009a). IBEX—Interstellar Boundary

Explorer. *Space Science Reviews*, 146, 11. https://doi.org/10.1007/s11214-009-9499-4

McComas, D. J., Allegrini, F., Bochsler, P., et al. (2009b). Global Observations of the Interstellar Interaction from the Interstellar Boundary Explorer (IBEX). *Science*, 326, 959. https://doi.org/10.1126/science.1180906

McComas, D. J., Lewis, W. S., & Schwadron, N. A. (2014). IBEX's Enigmatic Ribbon in the sky and its many possible sources. *Reviews of Geophysics*, 52,118–55. https://doi.org/10.1002/2013RG000438

McComas, D. J., Zirnstein, E. J., Bzowski, M., et al. (2017). Seven Years of Imaging the Global Heliosphere with IBEX. *The Astrophysical Journal Supplement Series*, 229, 41. https://doi.org/10.3847/1538-4365/aa66d8

McComas, D. J., Bzowski, M., Dayeh, M. A., et al. (2020). Solar Cycle of Imaging the Global Heliosphere: Interstellar Boundary Explorer (IBEX) Observations from 2009–2019. *The Astrophysical Journal Supplement Series*, 248, 26. https://doi.org/10.3847/1538-4365/ab8dc2

Min, K., & Liu, K. (2018). Contributions of Mirror and Ion Bernstein Instabilities to the Scattering of Pickup Ions in the Outer Heliosheath. *The Astrophysical Journal*, 852, 39. https://doi.org/10.3847/1538-4357/aaa0d4

Möbius, E., Liu, K., Funsten, H., Gary, S. P., & Winske, D. (2013). ANALYTIC MODEL OF THE IBEX RIBBON WITH NEUTRAL SOLAR WIND BASED ION PICKUP BEYOND THE HELIOPAUSE. *The Astrophysical Journal*, 766, 129. https://doi.org/10.1088/0004-637X/766/2/129

Mousavi, A., Liu, K., & Min, K. (2020). Mirror Instability Driven by Pickup Ions in the Outer Heliosheath. *The Astrophysical Journal*, 901, 167. https://doi.org/10.3847/1538-4357/abb1a1

NASA JPL. (n. d.). Voyager - The Interstellar Mission. Retrieved Oct 23, 2021, from
https://voyager.jpl.nasa.gov/mission/interstellar-mission/

NASA. (July 29, 2019). In Depth | Interstellar Boundary Explorer (IBEX) – NASA Solar System
Exploration. Retrieved Oct 23, 2021, from https://solarsystem.nasa.gov/missions/interstellar-
boundary-explorer-ibex/in-depth/

Niemiec, J., Florinski, V., Heerikhuisen, J., & Nishikawa, K.-I. (2016). THE IBEX RIBBON
AND THE PICKUP ION RING STABILITY IN THE OUTER HELIOSHEATH. II. MONTE-
CARLO AND PARTICLE-IN-CELL MODEL RESULTS. *The Astrophysical Journal*, 826, 198.
https://doi.org/10.3847/0004-637X/826/2/198

Opher, M. et al. (2020). A small and round heliosphere suggested by magnetohydrodynamic
modelling of pick-up ions. *Nature Astronomy*, 4, 675–683. https://doi.org/10.1038/s41550-020-
1036-0

Porazik, P., & Johnson J. R. (2013). Gyrokinetic particle simulation of nonlinear evolution of
mirror instability, *Journal of Geophysical Research Space Physics*, 118(11), 7211–7218.
https://doi.org/10.1002/2013JA019308

Richardson, J. D., Belcher, J. W., Garcia-Galindo, P., et al. (2019). Voyager 2 plasma
observations of the heliopause and interstellar medium. *Nature Astronomy*, 3, 1019.
https://doi.org/10.1038/s41550-019-0929-2

Ross, E., & Chaplin, W.J. (2019). The Behaviour of Galactic Cosmic-Ray Intensity During Solar
Activity Cycle 24. *Solar Physics*, 294, 8. https://doi.org/10.1007/s11207-019-1397-7

Roytershteyn, V., Pogorelov, N. V., & Heerikhuisen, J. (2019). Pickup Ions beyond the
Heliopause. *The Astrophysical Journal*, 881, 65. https://doi.org/10.3847/1538-4357/ab2ad4

Schwadron, N. A., Crew, G., Vanderspek, R., et al. (2009a). The interstellar boundary explorer science operations center, *Space Science Reviews*, 146, 207. https://doi.org/10.1007/s11214-009-9513-x

Schwadron, N. A., Bzowski, M., Crew, G. B., et al. (2009b). Comparison of Interstellar Boundary Explorer Observations with 3D Global Heliospheric Models. *Science*, 326, 966. https://doi.org/10.1126/science.1180986

Schwadron, N. A., & McComas, D. J. (2013). SPATIAL RETENTION OF IONS PRODUCING THE IBEX RIBBON. *The Astrophysical Journal*, 764, 92. https://doi.org/10.1088/0004-637X/764/1/92

Schwadron, N. A., & McComas, D. J. (2019). The Interstellar Ribbon: A Unifying Explanation. *The Astrophysical Journal*, 887, 247. https://doi.org/10.3847/1538-4357/ab5b91

Sheng, D., Liu, K., Florinski, V., & Perez J. D. (2021). Simulation of the Scattering of Continuously Injected Pickup Ions outside the Heliopause. Manuscript submitted for publication.

Summerlin, E. J., Vinas, A. F., Moore, T. E., Christian, E. R., & Cooper, J. F. (2014). ON THE STABILITY OF PICK-UP ION RING DISTRIBUTIONS IN THE OUTER HELIOSHEATH. *The Astrophysical Journal*, 793, 93. https://doi.org/10.1088/0004-637X/793/2/93

Zirnstein, E. J., Funsten, H. O., Heerikhuisen, J., et al. (2016). GEOMETRY AND CHARACTERISTICS OF THE HELIOSHEATH REVEALED IN THE FIRST FIVE YEARS OF INTERSTELLAR BOUNDARY EXPLORER OBSERVATIONS. *The Astrophysical Journal*, 826, 58. https://doi.org/10.3847/0004-637X/826/1/58

Zirnstein, E. J., Heerikhuisen, J., & Dayeh, M. A. (2018). The Role of Pickup Ion Dynamics Outside of the Heliopause in the Limit of Weak Pitch Angle Scattering: Implications for the

Source of the IBEX Ribbon. *The Astrophysical Journal*, 855, 30. https://doi.org/10.3847/1538-4357/aaaf6d

Zirnstein, E. J., Kim, T. K., Mostafavi, P., et al. (2020). Response of Pickup Ions in the Very Local Interstellar Medium to Solar Variations: Implications for the Evolution of the IBEX Ribbon and Interstellar Helium. *The Astrophysical Journal*, 91, 56. https://doi.org/10.3847/1538-4357/ab744b

Zank, G. (1999). Interaction of the solar wind with the local interstellar medium: a theoretical perspective. *Space Science Reviews*, 89, 413–688. https://doi.org/10.1023/A:1005155601277

Appendices

X1. Ambient fluctuations

A factor that impacts the scattering time is the timescale of the initial waves that are generated from instabilities which depend on the randomness of the initial condition. The simulation relies on artificial randomness and granularity of simulated particles and expects the timescale of this process to be short enough so that the initial randomness is less significant after the growth of waves. However, the fluctuations of the magnetic field energy in the simulations described above are lower than the observed ambient fluctuations in the outer heliopause region for a significant time period. This suggests that the ambient turbulence should be added to the simulation, to see whether it will affect the scattering time. Here we simply describe the method of implementing ambient turbulence as well as the preliminary results to show the wave growth with the presence of ambient turbulence. This is the prelude to future work.

Fraternale et a. (2019) shows that the power spectrum of ambient turbulence observed by Voyager 1 and 2 is Kolmogorov-like, with a power-law of fluctuation energies $E \propto k^{-5/3}$. If the parallel compressible component that doesn't participate in the PUIs scattering is ignored, the turbulence can be seen as the combination of the slab (parallel propagating) Alfvén waves and 2D non-propagating structures with its wave vector $\mathbf{k}$ perpendicular to $\mathbf{B_0}$. The energy ratio is 60% 2D and 40% slab according to Voyager 1 observations (Fraternale, 2019). To represent the ambient turbulence, random Alfvén waves described by Giacalone and Jokipii (1994) and Giacalone and Ellison (2000) could be generated at the beginning of the simulation. The 2D non-propagating structures, regarded as the Alfvén waves with $\pi/2$ angles theta between $\mathbf{k}$ and $\mathbf{B_0}$ and zero frequency, would be also implemented in the same way. Since the system is discrete, the wavenumber k_x and k_y for both turbulences are discretized to the eigenvalue of integer multiples

of $2\pi/(Nx\Delta x)$ and $2\pi/(Ny\Delta y)$ to satisfy the periodic boundary condition. The initial energy of the ambient turbulence in the frequency range of our simulation box is set as magnetic field energy of $4 \times 10^{-4}\ B_0^2$ and dissipated into the kinetic energy of particles as the system evolves as expected.

See Figure A1 and Figure A2, with the initial realistic ambient turbulence and artificial inject rate of PUIs, the evolution of energies is slightly changed, but there is no significant effect of ambient fluctuations on the growth of instabilities and PUIs scattering time. However, the added effect is still unknown if a more realistic injection rate is used. More research is needed.

Fraternale, F. et al. (2019). Magnetic Turbulence Spectra and Intermittency in the Heliosheath and in the Local Interstellar Medium. *ApJ*, 872, 40. https://doi.org/10.3847/1538-4357/aafd30

Giacalone J., & Jokipii, J. R. (1994). Charged-particle motion in multidimensional magnetic-field turbulence. *Astrophysical Journal Letters*. *430*, L137. https://doi.org/10.1086/187457

Giacalone J. & Ellison, D. C. (2000). Three-dimensional numerical simulations of particle injection and acceleration at quasi-perpendicular shocks. *Journal of Geophysical Research*. 105(A6), 12541. https://doi.org/10.1029/1999JA000018
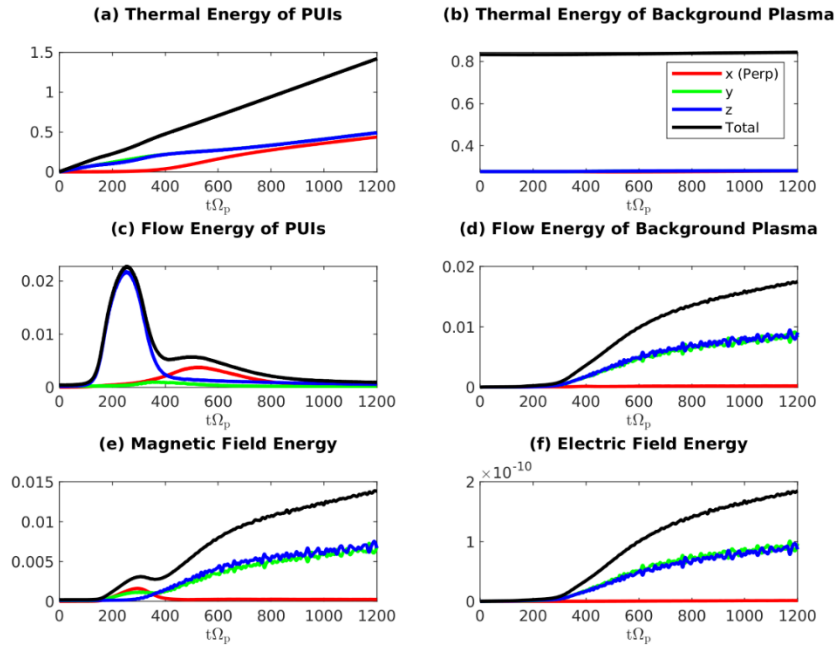
Figure A1. Time evolution of (a) PUI thermal energy, (b) Background plasma thermal energy, (c) PUI bulk flow energy, (d) Background plasma bulk flow energy, (e) magnetic field energy and (f) electric field energy, in units of $B_0^2/(2\mu_0)$, with initialized ambient fluctuations, with the same parameters as Figure 16.

Figure A2. The spatial form of the y component of the magnetic field fluctuations (left column) and the logarithm of the corresponding wave number power spectra (right column) as a function of k_x and k_y for $t\Omega_p =$ 200, 300, 400, 600, with initialized ambient fluctuations, with the same parameters as Figure 16.
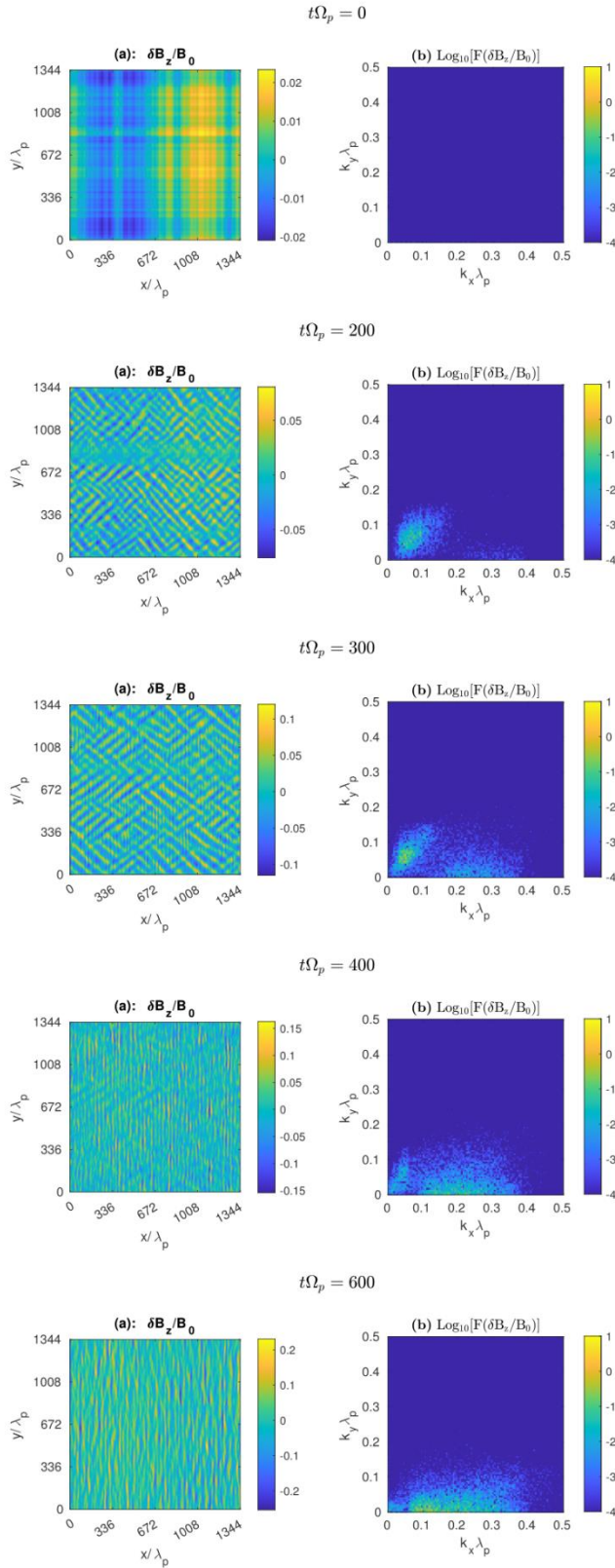
Postscript

Since the COVID breakout in 2019, our daily life has changed a lot. When I written the dissertation in late 2021, the consistent struggle with the pandemic is far from end. Humans entered a new era, the pandemic era, which is long forgotten in history. It forces people to realize the fragility of society, the inability of the global system, and the precious value of the connection between people.

Beware, the last centuries of rapid growth of the global economy, as well as the rise of the living standard of normal people, was a short period in million years of human history. In my humble opinion, it is the result of three waves of revolutions of science and technology (Mechanization, Electrification, Microelectronics). The economy of many developed countries has stagnated long ago since they moved the industry out, while their people are satisfied with the new toys of technology from Big Tech and cheap goods from outside of the country. However, those will easily disappear without a fourth wave of technology revolution, as how Moore's Law failed a few years ago.

Science research is like picking apples from the apple tree. The predecessors simply picked the apples in lower branches, leaving it more difficult for successor to pick apple in the higher branches. As a result, the development of modern science is less relevant to the talent of a scientist, but heavily relies on the development of new technologies. While the development of new technologies also requires new science. It is the circulation process. The problem is the circulation has bottle necks. The keep delaying of ITER (international nuclear fusion research) and NASA's new moon landing program are dangerous signs of stagnation.

In the past, the development of technologies was driven by the super high profit and demand from colonialism, imperialism or by the hysterical fear of war of annihilation (the internet was

created in the military to survive a nuclear war). They are against humanity and none of them are sustainable. We then went into an era of globalization (free capital flow and industrial transfer). It is an era of peace, full of amusement as well as idiocracy, but without awareness of danger, without considering who pays the cost. The economic crisis and pandemic just exposed reality. It is not surprising, one day we witness the collapse of globalization, at least of current form. The question is what will come next? I leave this question to the reader.

Decades ago, people had dreams like at the beginning of the 21st century, millions of people daily travel, work and live in space, when the earth is too small to be divided. I still hold the same dreams. I believe the next stage of evolution and the next chance for humans is the era of space. The time is crucial before the window for space exploration closes. I wish what I am working for attribute to those dreams.

Finally, pay honor to all the health workers and all these heroes who help fight the pandemic!